

# A Novel Overactuated Quadrotor Unmanned Aerial Vehicle: Modeling, Control, and Experimental Validation

Markus Ryll, Heinrich H. Bülfhoff, *Member, IEEE*, and Paolo Robuffo Giordano, *Member, IEEE*

**Abstract**—Standard quadrotor unmanned aerial vehicles (UAVs) possess a limited mobility because of their inherent underactuation, that is, availability of four independent control inputs (the four propeller spinning velocities) versus the 6 degrees of freedom parameterizing the quadrotor position/orientation in space. Thus, the quadrotor pose cannot track arbitrary trajectories in space (e.g., it can hover on the spot only when horizontal). Because UAVs are more and more employed as service robots for interaction with the environment, this loss of mobility due to their underactuation can constitute a limiting factor. In this paper, we present a novel design for a quadrotor UAV with tilting propellers which is able to overcome these limitations. Indeed, the additional set of four control inputs actuating the propeller tilting angles is shown to yield full actuation to the quadrotor position/orientation in space, thus allowing it to behave as a fully actuated flying vehicle. We then develop a comprehensive modeling and control framework for the proposed quadrotor, and subsequently illustrate the hardware and software specifications of an experimental prototype. Finally, the results of several simulations and real experiments are reported to illustrate the capabilities of the proposed novel UAV design.

**Index Terms**—Aerial robotics, aerodynamical modeling, dynamical modeling, flight control, overactuation, quadrotor unmanned aerial vehicles (UAVs), redundancy resolution.

## I. INTRODUCTION

COMMON unmanned aerial vehicles (UAVs) are underactuated mechanical systems, that is, systems possessing less control inputs than available degrees of freedom (DoF). This is, for instance, the case of helicopters and quadrotor UAVs for which only the Cartesian position and yaw angle with respect to an inertial frame can be independently controlled (4 DoF), whereas the behavior of the remaining roll and pitch angles (2 DoF) is completely determined by the trajectory chosen for the former 4 DoF (the so-called quadrotor flat outputs [1]–[3]).

Manuscript received August 19, 2013; revised March 5, 2014; accepted May 18, 2014. Date of publication July 30, 2014; date of current version February 11, 2015. Manuscript received in final form June 10, 2014. Recommended by Associate Editor L. Marconi.

M. Ryll is with Max Planck Institute for Biological Cybernetics, Tübingen 72076, Germany (e-mail: markus.ryll@tuebingen.mpg.de).

H. H. Bülfhoff is with Max Planck Institute for Biological Cybernetics, Tübingen 72076, Germany, and also with the Department of Brain and Cognitive Engineering, Korea University, Seoul 136-713, Korea (e-mail: hhb@tuebingen.mpg.de).

P. Robuffo Giordano is with the CNRS, Irisa and Inria Rennes Bretagne Atlantique, Rennes Cedex 35042, France (e-mail: prg@irisa.fr).

Color versions of one or more of the figures in this paper are available online at <http://ieeexplore.ieee.org>.

Digital Object Identifier 10.1109/TCST.2014.2330999

Over the last decades, a variety of control techniques have been proposed to deal with the quadrotor underactuation to allow for an effective and robust flight performance (see [3]–[5] for an overview). The constant improvements during the miniaturization of microelectromechanical systems and sensors (MEMS) and during the computational power of microcontrollers have led to impressive achievements by employing quadrotor UAVs as robotics platforms: planning and control for aggressive flight maneuvers [6], collective control of multiple small- and micro-quadrotors [7], [8], and vision-based state estimation for autonomous flight [9] are just a few examples.

Nevertheless, the underactuated quadrotor design still limits its flying ability in free or cluttered space, and it also degrades the possibility of interacting with the environment by exerting desired forces in arbitrary directions. This is a particularly a limiting factor because quadrotor UAVs are being more and more envisaged and exploited as autonomous flying service robots, for example, as proven by the recently funded EU projects AIRobots [10] and ARCAS [11]. Indeed, several groups have been addressing the possibility to allow for an actual interaction with the environment, either in the form of direct contact [12]–[14] or by considering aerial grasping and manipulation tasks [15]–[19]. In this respect, as also recognized in [20] and [21], it is interesting to explore different actuation strategies that can overcome the aforementioned underactuation problem and allow for full motion and force control in all directions in space.

Motivated by these considerations, several solutions have been proposed in the past literature spanning different concepts as, for example, tilt-wing mechanisms [22], [23], UAVs with nonparallel (but fixed) thrust directions [24], or tilt-rotor actuators [25], [26]. In [27], the possibility of combining several modules of underactuated ducted-fan vehicles to achieve full 6-dof actuation for the assembled robot is theoretically explored, with a special focus on the optimal allocation of the available (redundant) control inputs. In contrast, Hua *et al.* [20] consider the possibility of a thrust-tilted quadrotor UAV in which the main thrust direction (2 DoF) can be actively regulated. A trajectory tracking control strategy is then proposed, which is able to explicitly consider a limited range of the thrust-tilting angles. Finally, in [21] a UAV made of two central coaxial counter-rotating propellers surrounded by three tilting thrusters has been presented along with some preliminary experimental results. The prototype is capable of two flight modalities: a fixed configuration in which it



Fig. 1. Picture of the holocopter prototype. The four propeller groups are slightly tilted. Red bar: positive direction of the  $X_B$  holocopter body axis.

essentially behaves as a standard underactuated UAV, and a variable angle configuration which guarantees some degree of full actuation as shown in the reported results.

#### A. Paper Contributions

Taking inspiration from these works, in this paper we focus on a novel actuation concept for a quadrotor UAV in which all the (usually fixed) propellers are allowed to tilt about the axes connecting them to the main body frame [28]–[30]. Indeed, as explained, one of the limitations of the classical quadrotor design depends on its inherent underactuation: presence of only four independent control inputs (the four propeller spinning velocities) does not allow to independently control the position and orientation of the quadrotor at the same time. For instance, in quasi-hover conditions, an horizontal translation necessarily implies a change in the attitude or, symmetrically, a quadrotor can hover in place only when being horizontal with respect to the ground plane. In contrast, in this paper we will show that, by means of the additional four actuated tilting DoF, it is possible to gain full controllability over the quadrotor position and orientation, thus transforming it, as a matter of fact, in a fully actuated flying rigid body.<sup>1</sup> Fig. 1 shows a picture of our current prototype of quadrotor with tilting propellers, which will be denoted as holocopter throughout the following developments.

The rest of this paper, as well as its main contributions, are then organized as follows.

- 1) A complete dynamical model of the holocopter is first derived in Section II by considering the dominant aerodynamic forces and torques (the propeller actuation), and by analyzing the effects of the main neglected terms.
- 2) A trajectory tracking controller is then presented in Section III aimed at exploiting the actuation capabilities of the holocopter for tracking arbitrary trajectories for its body position and orientation. As the holocopter is actually overactuated (eight control inputs for six controlled DoF), suitable strategies to exploit the actuation redundancy are also discussed; these are aimed at preserving full controllability of the holocopter pose and at minimizing the total energy consumption during flight.

<sup>1</sup>This, of course, without considering possible limitations of the actuation systems such as, for example, finite range for the tilting angles. Section IV-A will further discuss these points with respect to the experimental prototype considered in this paper.

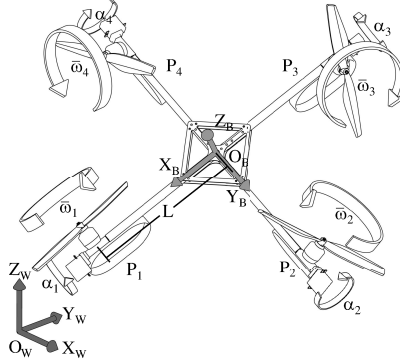


Fig. 2. Schematic view of the quadrotor considered in this paper. The overall center of mass is assumed to be in the body frame center. The symbol  $L$  represents the length of all propeller arms,  $\omega_i$ ,  $i = 1, \dots, 4$ , the propeller rotation speed and  $\alpha_i$ ,  $i = 1, \dots, 4$ , and the orientation of the propeller group.

- 3) A thorough description of the hardware/software architecture of the prototype shown in Fig. 1 is then given in Section IV, including the identification of its dynamical parameters and a discussion of the main nonidealities with respect to the dynamical model developed in Section II. In particular, a predictive scheme complementing the control action described in Section III is introduced to cope with the poor performance of the employed servo motors.
- 4) An extensive set of ideal/realistic simulations and experimental results on the holocopter prototype is then presented in Sections V–VII, showing the appropriateness of the various modeling assumptions and of the adopted control design. A video collecting several experimental flights is also attached to this paper.
- 5) Conclusions and some future discussions are then given in Section VII with a particular focus on the second-generation holocopter prototype currently under development.

## II. DYNAMICAL MODELING OF THE HOLOCOPTER

The quadrotor analyzed in this paper can be considered as a connection of 5 main rigid bodies in relative motion among themselves: the quadrotor body itself  $B$  and the 4 propeller groups  $P_i$ . These consist of the propeller arm hosting the motor responsible for the tilting actuation mechanism, and the propeller itself connected to the rotor of the motor responsible for the propeller spinning actuation<sup>2</sup> (see Figs. 1–3). The aim of this section is to derive the equations of motion of this multibody system.

#### A. Preliminary Definitions

Let  $\mathcal{F}_W : \{O_W; X_W, Y_W, Z_W\}$  be a world inertial frame and  $\mathcal{F}_B : \{O_B; X_B, Y_B, Z_B\}$  a moving frame attached to the quadrotor body at its center of mass (see Fig. 2). We also define  $\mathcal{F}_{P_i} : \{O_{P_i}; X_{P_i}, Y_{P_i}, Z_{P_i}\}$ ,  $i = 1, \dots, 4$ , as the frames associated to the  $i$ th propeller group, with  $X_{P_i}$

<sup>2</sup>For simplicity, we are here considering each propeller groups  $P_i$  as a single-body approximation of both the propeller/rotor and its hoisting mechanism.

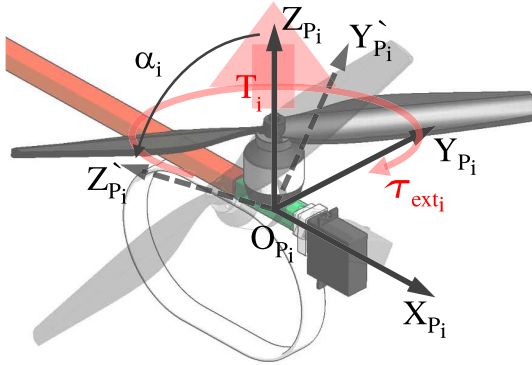


Fig. 3.  $i$ -th tilting arm visualizing the body frame  $\mathcal{F}_{P_i}$ , the associated propeller thrust  $T_i$ , torque  $\tau_{\text{ext}_i}$ , and the propeller tilt angle  $\alpha_i$ .

representing the tilting actuation axis and  $Z_{P_i}$  the propeller-actuated spinning (thrust  $T_i$ ) axis (see Fig. 3).

As usual, we let  ${}^1\mathbf{R}_2 \in SO(3)$  be the rotation matrix representing the orientation of frame 2 with respect to frame 1; therefore,  ${}^W\mathbf{R}_B$  will represent the orientation of the body frame with respect to the world frame, while  ${}^B\mathbf{R}_{P_i}$  the orientation of the propeller group  $i$ th frame with respect to the body frame. By denoting with  $\alpha_i \in \mathbb{R}$  the propeller tilt angle about axis  $X_{P_i}$ , it follows from Fig. 2 that:<sup>3</sup>

$${}^B\mathbf{R}_{P_i} = \mathbf{R}_Z \left( (i-1) \frac{\pi}{2} \right) \mathbf{R}_X(\alpha_i), \quad i = 1, \dots, 4.$$

Similarly, we also let

$${}^B\mathbf{O}_{P_i} = \mathbf{R}_Z \left( (i-1) \frac{\pi}{2} \right) \begin{bmatrix} L \\ 0 \\ 0 \end{bmatrix}, \quad i = 1, \dots, 4$$

be the origin of the propeller frames  $\mathcal{F}_{P_i}$  in the body frame with  $L$  being the distance of  $\mathbf{O}_{P_i}$  from  $\mathbf{O}_B$ .

Summarizing, the quadrotor configuration is completely determined by the body position  $\mathbf{p} = {}^W\mathbf{O}_B \in \mathbb{R}^3$  and orientation  ${}^W\mathbf{R}_B$  in the world frame, and by the four tilt angles  $\alpha_i$  specifying the propeller group orientations in the body frame (rotations about  $X_{P_i}$ ). We omit the propeller spinning angles about  $Z_{P_i}$  as configuration variables, although the propeller spinning velocities  $\bar{w}_i$  about  $Z_{P_i}$  will be part of the system model (see the following sections).

### B. Equations of Motion

By exploiting standard techniques (e.g., Newton–Euler procedure), it is possible to derive a complete description of the quadrotor dynamic model by considering the forces/momenta generated by the propeller motion, as well as any cross coupling due to gyroscopic and inertial effects arising from the relative motion of the five bodies composing the quadrotor. As aerodynamic forces/torques, we will only consider those responsible for the quadrotor actuation and neglect any additional second-order effects/disturbances. Indeed, as discussed in the next Section II-C, for the typical slow flight regimes considered in this paper, the propeller actuation forces/torques result significantly dominant with

<sup>3</sup>Throughout the following,  $\mathbf{R}_X(\theta)$ ,  $\mathbf{R}_Y(\theta)$ ,  $\mathbf{R}_Z(\theta)$  will denote the canonical rotation matrixes about the  $X$ ,  $Y$ ,  $Z$  axes of angle  $\theta$ , respectively.

respect to other aerodynamic effects. We now discuss in detail the main conceptual steps needed to derive the quadrotor dynamical model.

To this end, let  $\boldsymbol{\omega}_B \in \mathbb{R}^3$  be the angular velocity of the quadrotor body  $B$  expressed in the body frame,<sup>4</sup> and consider the  $i$ -th propeller group  $P_i$ . The angular velocity of the  $i$ -th propeller (i.e., of  $\mathcal{F}_{P_i}$ ) with respect to  $\mathcal{F}_W$  and expressed in  $\mathcal{F}_{P_i}$  is just

$$\boldsymbol{\omega}_{P_i} = {}^B\mathbf{R}_{P_i}^T \boldsymbol{\omega}_B + [\dot{\alpha}_i \ 0 \ \bar{w}_i]^T$$

where  $\dot{\alpha}_i$  is the tilting velocity about  $X_{P_i}$  and  $\bar{w}_i \in \mathbb{R}$  is the spinning velocity about  $Z_{P_i}$ , both with respect to  $\mathcal{F}_B$  (see Section II-A). This results in an angular acceleration

$$\dot{\boldsymbol{\omega}}_{P_i} = {}^B\mathbf{R}_{P_i}^T \dot{\boldsymbol{\omega}}_B + {}^B\dot{\mathbf{R}}_{P_i}^T \boldsymbol{\omega}_B + [\ddot{\alpha}_i \ 0 \ \dot{\bar{w}}_i]^T.$$

By applying the Euler equations of motion, it follows that:

$$\mathbf{T}_{P_i} = \mathbf{I}_{P_i} \dot{\boldsymbol{\omega}}_{P_i} + \boldsymbol{\omega}_{P_i} \times \mathbf{I}_{P_i} \boldsymbol{\omega}_{P_i} - \boldsymbol{\tau}_{\text{ext}_i}. \quad (1)$$

Here,  $\mathbf{I}_{P_i} \in \mathbb{R}^{3 \times 3}$  is the (constant) symmetric and positive definite inertia matrix of the  $i$ -th propeller/rotor assembly approximated as an equivalent disc (the inertia of the tilting mechanism is supposed lumped into the main body  $B$ ), and  $\boldsymbol{\tau}_{\text{ext}_i}$  any external torque applied to the propeller. As usual, see, for example, [31], we assume presence of a counter-rotating torque about the  $Z_{P_i}$  axis caused by air drag and modeled as

$$\boldsymbol{\tau}_{\text{ext}_i} = [0 \ 0 \ -k_m \omega_{P_i Z} |\omega_{P_i Z}|]^T, \quad k_m > 0 \quad (2)$$

with  $\omega_{P_i Z}$  being the third component of  $\boldsymbol{\omega}_{P_i}$ .

Let now

$$\mathbf{T}_{P_i} = [0 \ 0 \ k_f \bar{w}_i |\bar{w}_i|]^T, \quad k_f > 0 \quad (3)$$

represent the  $i$ -th propeller force (thrust) along the  $Z_{P_i}$  axis and acting at  ${}^B\mathbf{O}_{P_i}$  in  $\mathcal{F}_B$ . By considering the quadrotor body  $B$  and the torques generated by the four propellers  $P_i$ , one then obtains

$$\sum_{i=1}^4 \left( {}^B\mathbf{O}_{P_i} \times {}^B\mathbf{R}_{P_i} \mathbf{T}_{P_i} - {}^B\mathbf{R}_{P_i} \boldsymbol{\tau}_{P_i} \right) = \mathbf{I}_B \dot{\boldsymbol{\omega}}_B + \boldsymbol{\omega}_B \times \mathbf{I}_B \boldsymbol{\omega}_B \quad (4)$$

with  $\mathbf{I}_B \in \mathbb{R}^{3 \times 3}$  being the (constant) symmetric and positive definite inertia matrix of  $B$ .

As for the translational dynamics, we assume for simplicity that the barycenter of each propeller group  $P_i$  coincides with  $\mathbf{O}_{P_i}$ . This allows us to neglect inertial effects on the propeller groups owing to the quadrotor body acceleration in space. Therefore, by recalling that  $\mathbf{p} = {}^W\mathbf{O}_B$  is the quadrotor body position in world frame, one has

$$m \ddot{\mathbf{p}} = m \begin{bmatrix} 0 \\ 0 \\ -g \end{bmatrix} + {}^W\mathbf{R}_B \sum_{i=1}^4 {}^B\mathbf{R}_{P_i} \mathbf{T}_{P_i} \quad (5)$$

where  $m$  is the total mass of the quadrotor and propeller bodies and  $g$  is the scalar gravitational acceleration of Earth.

<sup>4</sup>In the following, we will assume that every quantity is expressed in its own frame, for example,  $\boldsymbol{\omega}_B = {}^B\boldsymbol{\omega}_B$ .

TABLE I  
MAIN QUANTITIES AND DEFINITIONS FOR THE  
HOLOCOPTER DYNAMIC MODEL

Symbols	Definitions
$\mathcal{F}_W$	inertial world frame
$\mathcal{F}_B$	quadrotor body frame $B$
$\mathcal{F}_{P_i}$	$i$ -th propeller group frame $P_i$
$\mathbf{p}$	position of $B$ in $\mathcal{F}_W$
${}^W\mathbf{R}_B$	rotation matrix from $\mathcal{F}_B$ to $\mathcal{F}_W$
${}^B\mathbf{R}_{P_i}$	rotation matrix from $\mathcal{F}_{P_i}$ to $\mathcal{F}_B$
$\alpha_i$	$i$ -th propeller tilt angle about $\mathbf{X}_{P_i}$
$\bar{w}_i$	$i$ -th propeller spinning velocity about $\mathbf{Z}_{P_i}$
$\boldsymbol{\omega}_B$	angular velocity of $B$ in $\mathcal{F}_B$
$\tau_{ext,i}$	$i$ -th propeller air drag torque about $\mathbf{Z}_{P_i}$
$\mathbf{T}_i$	$i$ -th propeller thrust along $\mathbf{Z}_{P_i}$
$\tau_{T_i}$	motor torque actuating $\mathbf{X}_{P_i}$
$\tau_{\bar{w}_i}$	motor torque actuating $\mathbf{Z}_{P_i}$
$m$	total mass
$\mathbf{I}_P$	inertia of the $i$ -th propeller group $P_i$
$\mathbf{I}_B$	inertia of the quadrotor body $B$
$k_f$	propeller thrust coefficient
$k_m$	propeller drag coefficient
$L$	distance of $\mathcal{F}_{P_i}$ from $\mathcal{F}_B$
$g$	gravitational acceleration of Earth

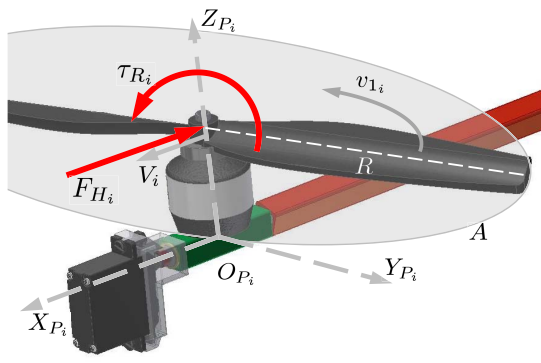


Fig. 4. Visualization of hub force  $\mathbf{F}_{H_i}$  and rolling moment  $\tau_{R_i}$  acting on a single blade.

Summarizing, (1)–(5) describe the rotational/translational dynamics of the quadrotor body and propeller groups. Note that the inputs of this model are the motor torques actuating the propeller tilting axes  $\mathbf{X}_{P_i}$  and spinning axes  $\mathbf{Z}_{P_i}$ . These are denoted as  $\tau_{\alpha_i} = \tau_{P_i}^T \mathbf{X}_{P_i} \in \mathbb{R}$  and  $\tau_{\bar{w}_i} = \tau_{P_i}^T \mathbf{Z}_{P_i} \in \mathbb{R}$ ,  $i = 1, \dots, 4$ , respectively, for a total of  $4 + 4 = 8$  independent control torques (inputs). The propeller spinning velocities  $\bar{w}_i$  (actuated by  $\tau_{\bar{w}_i}$ ) will then generate the forces and torques affecting the translational/rotational motion of the quadrotor body  $B$  as a function of its current configuration, in particular of the tilting angles  $\alpha_i$  actuated by  $\tau_{\alpha_i}$ . For the reader's convenience, Table I lists the main quantities introduced in this section.

### C. Additional Aerodynamic Effects

The derivation of the most significant aerodynamic effects besides the already considered propeller torques/forces (2–3) can be obtained by considering momentum and blade element theory. In this section, we will focus on the influence of the hub force  $\mathbf{F}_{H_i}$  (a force perpendicular to the rotor shaft acting on the single blade elements) and of the rolling moment  $\tau_{R_i}$  (a torque around  $\mathbf{X}_{P_i}$  caused by different thrust on the retreating and the

TABLE II  
SYMBOLS AND DEFINITIONS DESCRIBING THE MAIN  
AERODYNAMIC EFFECTS ON A SINGLE PROPELLER

Symbols	Definitions
$\rho$ [ $\text{kg}/\text{m}^3$ ]	Air density
$A$ [ $\text{m}^2$ ]	Propeller disk area
$v_1$ [ $\text{m}/\text{s}$ ]	Propeller inflow velocity
$\mathbf{F}_H$ [ $\text{N}$ ]	Hub force
$\tau_R$ [ $\text{Nm}$ ]	Rolling moment
$R$ [ $\text{m}$ ]	Propeller radius
$a$	Lift slope
$\sigma$ [ $\text{rad}^{-1}$ ]	Solidity ratio
$C_d$	Average drag coefficient
$\lambda_i$	Inflow ratio
$\mu_i$	Rotor advance ratio
$\theta_0$ [ $\text{rad}$ ]	Pitch of incidence
$\theta_{tw}$ [ $\text{rad}$ ]	Twist pitch
$\dot{x}_{P_i}, \dot{y}_{P_i}, \dot{z}_{P_i}$ [ $\text{m}/\text{s}$ ]	Velocity of the propeller w.r.t. ground

advancing blade of the propeller). Fig. 4 shows an illustration of these quantities, and Table II summarizes the main symbols introduced hereafter.

Let  $(\dot{x}_{P_i}, \dot{y}_{P_i}, \dot{z}_{P_i}) = {}^W\mathbf{R}_{P_i}^T {}^W\dot{\mathbf{O}}_{P_i}$  be the velocity of the  $i$ th propeller with respect to the world frame and expressed in the propeller frame  $\mathcal{F}_{P_i}$ . We define

$$V_i = \sqrt{\dot{x}_{P_i}^2 + \dot{y}_{P_i}^2}$$

as the sideways velocity of the  $i$ th propeller in propeller group frame. Momentum theory models the generated thrust of a single propeller as

$$\|\mathbf{T}_{P_i}\| = 2\rho A v_{1i} \sqrt{V_i^2 + v_{1i}^2},$$

with  $v_{1i}$  being the so-called  $i$ th propeller inflow velocity [32]. Solving for  $v_{1i}$  we get

$$v_{1i} = \sqrt{\frac{V_i^2}{2} + \sqrt{\left(\frac{V_i^2}{2}\right)^2 + \left(\frac{\|\mathbf{T}_{P_i}\|}{2\rho A}\right)^2}} \quad (6)$$

where  $\rho$  is the air density and  $A$  the rotor area.

Following the assumptions and simplifications of [33], the magnitude of the hub force  $\mathbf{F}_{H_i}$  can then be modeled as

$$\begin{cases} \|\mathbf{F}_{H_i}\| = C_{H_i} \rho A (\bar{w}_i R)^2 \\ \frac{C_{H_i}}{\sigma a} = \frac{1}{4a} \mu_i \bar{C}_d + \frac{1}{4} \lambda_i \mu_i \left( \theta_0 - \frac{\theta_{tw}}{2} \right) \end{cases} \quad (7)$$

where

$$\lambda_i = \frac{v_{1i} - \dot{z}_{P_i}}{\bar{w}_i R}, \quad \mu_i = \frac{V_i}{\bar{w}_i R} \quad (8)$$

and  $R$  is the propeller radius,  $\sigma$  is the solidity ratio,  $a$  is the lift slope,  $\bar{C}_d$  is the average drag coefficient,  $\theta_0$  is the pitch of incidence, and  $\theta_{tw}$  is the twist pitch. One can similarly model the magnitude of the rolling moment  $\tau_{R_i}$  acting on  $P_i$  and owing to the different lift of the retreating and the advancing blade of the propeller as

$$\begin{cases} \|\tau_{R_i}\| = C_{R_i} \rho A (\bar{w}_i R)^2 R \\ \frac{C_{R_i}}{\sigma a} = -\mu_i \left( \frac{1}{6} \theta_0 - \frac{1}{8} \theta_{tw} - \frac{1}{8} \lambda_i \right). \end{cases} \quad (9)$$

To assess the influence of these aerodynamic effects, we compared them with the thrust  $\mathbf{T}_{P_i}$  and torque  $\tau_{ext,i}$  of

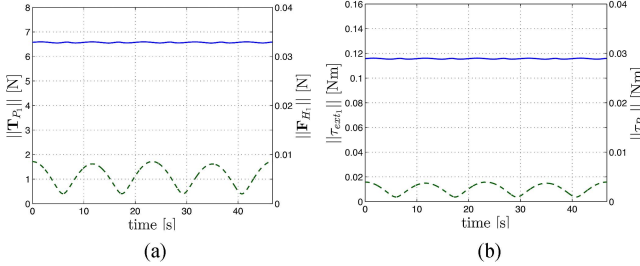


Fig. 5. (a) Solid line: thrust  $\|T_{P_1}\|$  in  $\mathcal{F}_{P_1}$  (left y-axis). Dashed line: hub force  $\|F_{H_1}\|$  in  $\mathcal{F}_{P_1}$  (right y-axis). (b) Solid line: drag  $\|\tau_{\text{ext}1}\|$  in  $\mathcal{F}_{P_1}$  (left y-axis). Dashed line: rolling moment  $\|\tau_{R_1}\|$  in  $\mathcal{F}_{P_1}$  (right y-axis). Note the different scales of the y-axes in both plots.

a single propeller during the simulated trajectory described in Section V-A 2 and relying, for the various parameters, on the physical properties of our prototype and on values taken from literature. The trajectory consists of a horizontal eight-shape planar curve with a superimposed sinusoidal rotation about the body  $Y_B$  axis, and has been chosen as being representative of the typical operational regimes of our prototype. The results are shown in Fig. 5: as clear from the plots, it is  $\|T_{P_1}\|/\|F_{H_1}\| \simeq 600$  and  $\|\tau_{\text{ext}1}\|/\|\tau_{R_1}\| \simeq 30$  (note the two different scales of the y-axes in both plots). This then confirms the minor significance of these (neglected) second-order aerodynamics effects with respect to the propeller actuation forces/torques (2) and (3) which are instead taken into account in the holocopter dynamical model. As for the significance of blade flapping and induced drag (typically modeled as the first-order contributions, see [3]), a similar analysis showed an even smaller effect with respect to the aforementioned second-order forces/torques in the same flying regimes. Therefore, these first-order terms were also neglected in the holocopter model.

### III. MOTION CONTROL OF THE HOLOCOPTER

We now proceed to illustrate the control approach adopted in this paper for exploiting the holocopter capabilities in tracking arbitrary desired trajectories for the position and orientation of its main body  $B$ .

#### A. Simplified Holocopter Model

We start with some preliminary considerations: the dynamic model illustrated in the previous section is useful for simulation purposes as it captures the main effects of the quadrotor motion in space (apart from unmodeled aerodynamics forces/torques). Some simplifications are, however, useful for transforming it into a reduced model more suited to control design. First, as in many practical situations, we assume that the motors actuating the tilting/spinning axes are implementing a fast high-gain local controller able to impose desired speeds  $w_{\alpha_i} = \dot{\alpha}_i$  and  $\bar{w}_i$  with negligible transients.<sup>5</sup> This allows to neglect the motor dynamics, and to consider  $w_{\alpha_i}$  and  $\bar{w}_i$ ,  $i = 1, \dots, 4$ , as (virtual) control inputs in place of the motor torques  $\tau_{\alpha_i}$  and  $\tau_{\bar{w}_i}$ . Second, in this simplified model we

<sup>5</sup>For instance, in the standard quadrotor case, the spinning velocities  $\bar{w}_i$  are usually taken as control inputs.

also neglect the internal gyroscopic/inertial effects by considering them as second-order disturbances to be rejected by the controller.<sup>6</sup> We note that the validity of these assumptions will be discussed in Section V-A where the proposed controller will be tested against the complete dynamic model described in Section II representing the actual dynamics of the quadrotor.

Let us then define  $\boldsymbol{\alpha} = [\alpha_1, \dots, \alpha_4]^T \in \mathbb{R}^4$ ,  $\mathbf{w}_\alpha = [w_{\alpha_1}, \dots, w_{\alpha_4}]^T \in \mathbb{R}^4$  and  $\mathbf{w} = [\bar{w}_1|\bar{w}_1|, \dots, \bar{w}_4|\bar{w}_4|]^T \in \mathbb{R}^4$ . Note that the elements of vector  $\mathbf{w}$  are the signed squares of the spinning velocities  $\bar{w}_i$ , as the torques and forces in (2) and (3) are a (approx. linear) function of these quantities. Therefore, in the following analysis,  $w_i = \bar{w}_i|\bar{w}_i|$  will be considered as input spinning velocity of the  $i$ th propeller, with the understanding that one can always recover the actual speed  $\bar{w}_i = \text{sign}(w_i)\sqrt{|w_i|}$ . Under the stated assumptions, the quadrotor dynamic model can be simplified into

$$\begin{cases} \ddot{\mathbf{p}} = \begin{bmatrix} 0 \\ 0 \\ -g \end{bmatrix} + \frac{1}{m} {}^W \mathbf{R}_B \mathbf{F}(\boldsymbol{\alpha}) \mathbf{w} \\ \dot{\mathbf{w}}_B = \mathbf{I}_B^{-1} \boldsymbol{\tau}(\boldsymbol{\alpha}) \mathbf{w} \\ \dot{\boldsymbol{\alpha}} = \mathbf{w}_\alpha \\ {}^W \dot{\mathbf{R}}_B = {}^W \mathbf{R}_B [\boldsymbol{\omega}_B]_\wedge \end{cases} \quad (10)$$

with  $[\cdot]_\wedge$  being the usual map taking a vector  $\boldsymbol{\alpha} \in \mathbb{R}^3$  into the associated skew-symmetric matrix  $[\boldsymbol{\alpha}]_\times \in so(3)$ , and

$$\begin{aligned} \mathbf{F}(\boldsymbol{\alpha}) &= \begin{bmatrix} 0 & -k_f s_2 & 0 & k_f s_4 \\ -k_f s_1 & 0 & k_f s_3 & 0 \\ k_f c_1 & -k_f c_2 & k_f c_3 & -k_f c_4 \end{bmatrix} \\ \boldsymbol{\tau}(\boldsymbol{\alpha}) &= \begin{bmatrix} 0 & -Lk_f c_2 - k_m s_2 \\ -Lk_f c_1 + k_m s_1 & 0 \\ -Lk_f s_1 - k_m c_1 & Lk_f s_2 - k_m c_2 \\ 0 & Lk_f c_4 + k_m s_4 \\ Lk_f c_3 - k_m s_3 & 0 \\ -Lk_f s_3 - k_m c_3 & Lk_f s_4 - k_m c_4 \end{bmatrix} \end{aligned} \quad (11)$$

the  $3 \times 4$  input coupling matrixes ( $s_i = \sin(\alpha_i)$  and  $c_i = \cos(\alpha_i)$ ). Note that input  $\mathbf{w}$  appears linearly in (10) as expected. The subsequent control design is then performed on the simplified model (10) and (11).

#### B. Control Design

The control problem considered in this paper is an output-tracking problem: how to track, with the available inputs, a desired (and arbitrary) trajectory  $(\mathbf{p}_d(t), \mathbf{R}_d(t)) \in \mathbb{R}^3 \times SO(3)$  for the body position  $\mathbf{p}$  and orientation  ${}^W \mathbf{R}_B$  taken as output functions. We note again that this problem is clearly ill-posed for a standard quadrotor with fixed propellers because of its underactuation. However, the chosen overactuated design of the holocopter (eight independent control inputs) can guarantee full controllability over the position/orientation of its main body as it is shown in the following developments.

As in many output-tracking problems, a possible solution is to resort to output feedback linearization techniques

<sup>6</sup>Obviously, this assumption holds as long as the inertia of the propeller group is small with respect to the main holocopter body.

(either static or dynamic, see [34] for a detailed treatment). Therefore, we rewrite the first two rows of (10) as

$$\begin{aligned} \begin{bmatrix} \ddot{\mathbf{p}} \\ \dot{\boldsymbol{\omega}}_B \end{bmatrix} &= \begin{bmatrix} \begin{bmatrix} 0 \\ 0 \\ -g \\ \mathbf{0} \end{bmatrix} \\ \frac{1}{m} \mathbf{R}_B \quad \mathbf{0} \\ \mathbf{0} \quad \mathbf{I}_B^{-1} \end{bmatrix} \begin{bmatrix} \mathbf{F}(\boldsymbol{\alpha}) \quad \mathbf{0} \\ \boldsymbol{\tau}(\boldsymbol{\alpha}) \quad \mathbf{0} \end{bmatrix} \begin{bmatrix} \mathbf{w} \\ \mathbf{w}_\alpha \end{bmatrix} \\ &= \mathbf{f} + \mathbf{J}_R [\bar{\mathbf{J}}_\alpha(\boldsymbol{\alpha}) \quad \mathbf{0}] \begin{bmatrix} \mathbf{w} \\ \mathbf{w}_\alpha \end{bmatrix} \\ &= \mathbf{f} + \mathbf{J}_R \mathbf{J}_\alpha(\boldsymbol{\alpha}) \begin{bmatrix} \mathbf{w} \\ \mathbf{w}_\alpha \end{bmatrix} \\ &= \mathbf{f} + \mathbf{J}(\boldsymbol{\alpha}) \begin{bmatrix} \mathbf{w} \\ \mathbf{w}_\alpha \end{bmatrix} \end{aligned} \quad (12)$$

where  $\mathbf{f} \in \mathbb{R}^6$  is a constant drift vector,  $\bar{\mathbf{J}}(\boldsymbol{\alpha}) \in \mathbb{R}^{6 \times 4}$ ,  $\mathbf{J}_R \in \mathbb{R}^{6 \times 6}$ , and the  $6 \times 8$  matrix  $\mathbf{J}(\boldsymbol{\alpha})$  will be referred to as the output Jacobian. When  $\rho_J = \text{rank}(\mathbf{J}(\boldsymbol{\alpha})) = 6$ , it is always possible to statically feedback linearize (12) by means of the law

$$\begin{bmatrix} \mathbf{w} \\ \mathbf{w}_\alpha \end{bmatrix} = \mathbf{K}(\boldsymbol{\alpha}) \left( -\mathbf{f} + \begin{bmatrix} \ddot{\mathbf{p}}_r \\ \dot{\boldsymbol{\omega}}_r \end{bmatrix} \right) \quad (13)$$

where  $\mathbf{K}(\boldsymbol{\alpha})$  is a generalized inverse of  $\mathbf{J}(\boldsymbol{\alpha})$ , for example, the pseudoinverse  $\mathbf{J}^\dagger(\boldsymbol{\alpha})$ , and  $[\ddot{\mathbf{p}}_r^T \quad \dot{\boldsymbol{\omega}}_r^T]^T \in \mathbb{R}^6$  an arbitrary reference linear/angular acceleration vector to be imposed to the output dynamics in (10).

This solution is, however, not viable in the case under consideration. Indeed,  $\rho_J = \text{rank}(\mathbf{J}) = \text{rank}(\mathbf{J}_R \mathbf{J}_\alpha) = \text{rank}(\mathbf{J}_\alpha)$  since  $\mathbf{J}_R$  is a nonsingular square matrix. Furthermore,  $\rho_J = \text{rank}(\mathbf{J}_\alpha) = \text{rank}(\bar{\mathbf{J}}_\alpha) \leq 4 < 6$  because of the structural null matrix  $\mathbf{0} \in \mathbb{R}^{6 \times 4}$  in matrix  $\mathbf{J}_\alpha(\boldsymbol{\alpha})$  weighting the inputs  $\mathbf{w}_\alpha$ . Presence of this null matrix is due to the fact that inputs  $\mathbf{w}_\alpha$  affect the output dynamics at a higher differential level compared with inputs  $\mathbf{w}$ . Therefore, a direct inversion at the acceleration level is bound to exploit only inputs  $\mathbf{w}$  resulting in a loss of controllability for the system. Intuitively, the instantaneous linear/angular acceleration of the quadrotor body is directly affected by the propeller speeds  $\mathbf{w}$  and tilting configuration  $\boldsymbol{\alpha}$  (thanks to the dependence in  $\bar{\mathbf{J}}_\alpha(\boldsymbol{\alpha})$ ), but not by  $\dot{\boldsymbol{\alpha}} = \mathbf{w}_\alpha$ , that is, the tilting velocities.<sup>7</sup>

A possible way to circumvent these difficulties is to resort to a dynamic output linearization scheme and seek to invert the input–output map at a higher differential level where inputs  $\mathbf{w}_\alpha$  will explicitly appear. This can be achieved by expanding the term  $\bar{\mathbf{J}}_\alpha(\boldsymbol{\alpha})\mathbf{w}$  in (12) as follows:

$$\bar{\mathbf{J}}_\alpha(\boldsymbol{\alpha})\mathbf{w} = \sum_{i=1}^4 \bar{\mathbf{j}}_i(\boldsymbol{\alpha}) w_i$$

and noting that

$$\frac{d\bar{\mathbf{J}}_\alpha(\boldsymbol{\alpha})\mathbf{w}}{dt} = \bar{\mathbf{J}}_\alpha(\boldsymbol{\alpha})\dot{\mathbf{w}} + \sum_{i=1}^4 \frac{\partial \bar{\mathbf{j}}_i(\boldsymbol{\alpha})}{\partial \boldsymbol{\alpha}} \mathbf{w}_\alpha w_i$$

<sup>7</sup>It is interesting to note that this inhomogeneity in the differential levels at which inputs are affecting the output dynamics is not a specificity of the system at hand. As an example, the same structural property is also present in other robotic structures such as mobile manipulators with steering wheels [35] where the role of  $\mathbf{w}_\alpha$  is played by the wheel steering velocities.

differentiation of (12) with respect to time yields

$$\begin{aligned} \begin{bmatrix} \ddot{\mathbf{p}} \\ \ddot{\boldsymbol{\omega}}_B \end{bmatrix} &= \mathbf{J}_R \bar{\mathbf{J}}_\alpha(\boldsymbol{\alpha})\dot{\mathbf{w}} + \mathbf{J}_R \sum_{i=1}^4 \frac{\partial \bar{\mathbf{j}}_i(\boldsymbol{\alpha})}{\partial \boldsymbol{\alpha}} \mathbf{w}_\alpha w_i + \mathbf{J}_R \bar{\mathbf{J}}_\alpha(\boldsymbol{\alpha})\mathbf{w} \\ &= \mathbf{J}_R \left[ \bar{\mathbf{J}}_\alpha(\boldsymbol{\alpha}) \sum_{i=1}^4 \frac{\partial \bar{\mathbf{j}}_i(\boldsymbol{\alpha})}{\partial \boldsymbol{\alpha}} w_i \right] \begin{bmatrix} \dot{\mathbf{w}} \\ \mathbf{w}_\alpha \end{bmatrix} + \begin{bmatrix} \frac{W\dot{\mathbf{R}}_B}{m} \mathbf{F}(\boldsymbol{\alpha})\mathbf{w} \\ \mathbf{0} \end{bmatrix} \end{aligned} \quad (14)$$

$$\begin{aligned} &= \mathbf{J}_R \mathbf{J}'_\alpha(\boldsymbol{\alpha}, \mathbf{w}) \begin{bmatrix} \dot{\mathbf{w}} \\ \mathbf{w}_\alpha \end{bmatrix} + \mathbf{b}(\boldsymbol{\alpha}, \mathbf{w}, \boldsymbol{\omega}_B) \\ &= \mathbf{A}(\boldsymbol{\alpha}, \mathbf{w}) \begin{bmatrix} \dot{\mathbf{w}} \\ \mathbf{w}_\alpha \end{bmatrix} + \mathbf{b}(\boldsymbol{\alpha}, \mathbf{w}, \boldsymbol{\omega}_B) \end{aligned} \quad (15)$$

where the new input  $\dot{\mathbf{w}}$  is the dynamic extension of the former (and actual) input  $\mathbf{w}$  obtained by adding four integrators on its channel.<sup>8</sup>

We note that the new  $6 \times 8$  input–output decoupling matrix  $\mathbf{A}(\boldsymbol{\alpha}, \mathbf{w})$  consists of two column blocks: although the first block  $\mathbf{J}_R \bar{\mathbf{J}}_\alpha(\boldsymbol{\alpha})$  is exactly the first block of the former output Jacobian  $\mathbf{J}(\boldsymbol{\alpha})$ , the second block is not a null matrix as in the previous case. Rather, a new set of 4 columns, weighting inputs  $\mathbf{w}_\alpha$ , are now present and contributing to the rank of matrix  $\mathbf{A}$ . Furthermore, it is  $\mathbf{A}(\boldsymbol{\alpha}, \mathbf{0}) = \mathbf{J}(\boldsymbol{\alpha})$  and, as proven in [28],  $\rho_A = \text{rank}(\mathbf{A}) = 6$  as long as  $w_i \neq 0$ ,  $i = 1 \dots 4$ ; in other words, full rankness of matrix  $\mathbf{A}$  can always be ensured by preventing the propellers from stopping their spinning motion. Section III-C proposes a strategy able to meet this requirement.

With  $\rho_A = \text{rank}(\mathbf{A}) = 6$  system (14) can be inverted by the law

$$\begin{bmatrix} \dot{\mathbf{w}} \\ \mathbf{w}_\alpha \end{bmatrix} = \mathbf{A}^\dagger \left( \begin{bmatrix} \ddot{\mathbf{p}}_r \\ \ddot{\boldsymbol{\omega}}_r \end{bmatrix} - \mathbf{b} \right) + (\mathbf{I}_8 - \mathbf{A}^\dagger \mathbf{A}) \mathbf{z} \quad (16)$$

with  $\mathbf{I}_N$  being the identity matrix of dimension  $N$  and  $\mathbf{A}^\dagger \in \mathbb{R}^{8 \times 6}$  denoting the Moore–Penrose pseudoinverse of matrix  $\mathbf{A}$ , to achieve full input–output linearization

$$\begin{bmatrix} \ddot{\mathbf{p}} \\ \ddot{\boldsymbol{\omega}}_B \end{bmatrix} = \begin{bmatrix} \ddot{\mathbf{p}}_r \\ \ddot{\boldsymbol{\omega}}_r \end{bmatrix}. \quad (17)$$

Vector  $\mathbf{z} \in \mathbb{R}^8$  in (16) is an additional free quantity projected onto the 2-D null-space of  $\mathbf{A}$  whose use will be detailed in Section III-C. We note that presence of a 2-D null space for matrix  $\mathbf{A}$  is a direct (and expected) consequence of the actuation redundancy of degree 2 of the considered holocopter (eight control inputs for 6 controlled DoF).

Assuming now  $\mathbf{p}_d(t) \in \mathcal{C}^3$ , it is then sufficient to set in (17)

$$\ddot{\mathbf{p}}_r = \ddot{\mathbf{p}}_d + \mathbf{K}_{p_1}(\ddot{\mathbf{p}}_d - \ddot{\mathbf{p}}) + \mathbf{K}_{p_2}(\dot{\mathbf{p}}_d - \dot{\mathbf{p}}) + \mathbf{K}_{p_3}(\mathbf{p}_d - \mathbf{p}) \quad (18)$$

for obtaining exponential and decoupled convergence of the position error to  $\mathbf{0}$  as long as the (diagonal) positive definite gain matrixes  $\mathbf{K}_{p_1}$ ,  $\mathbf{K}_{p_2}$ ,  $\mathbf{K}_{p_3}$  define Hurwitz polynomials. For the stabilization of the orientation-tracking error, several choices are possible depending on the particular parameterization chosen for the rotation matrix  $\mathbf{R}$ . Besides the usual

<sup>8</sup>By means of this dynamic extensions, vector  $\mathbf{w}$  becomes an internal state of the controller.

Euler angles (with their inherent singularity issues), a convenient possibility is to resort to an orientation error term directly defined on  $SO(3)$  (as shown in [36] and [37]). Assume, as before, that  $\mathbf{R}_d(t) \in \bar{\mathcal{C}}^3$  and let  $\boldsymbol{\omega}_d = [\mathbf{R}_d^T \dot{\mathbf{R}}_d]_{\vee}$ , where  $[\cdot]_{\vee}$  represents the inverse map from  $so(3)$  to  $\mathbb{R}^3$ . By defining the orientation error as

$$\boldsymbol{e}_R = \frac{1}{2} [\mathbf{R}_B^T \mathbf{R}_d - \mathbf{R}_d^T \mathbf{R}_B]_{\vee} \quad (19)$$

the choice

$$\ddot{\boldsymbol{\omega}}_r = \ddot{\boldsymbol{\omega}}_d + \mathbf{K}_{\omega_1}(\dot{\boldsymbol{\omega}}_d - \dot{\boldsymbol{\omega}}_B) + \mathbf{K}_{\omega_2}(\boldsymbol{\omega}_d - \boldsymbol{\omega}_B) + \mathbf{K}_{\omega_3}\boldsymbol{e}_R \quad (20)$$

in (17) yields an exponential convergence for the orientation-tracking error to  $\mathbf{0}$  as desired, provided that the (diagonal) gain matrixes  $\mathbf{K}_{\omega_1}$ ,  $\mathbf{K}_{\omega_2}$ ,  $\mathbf{K}_{\omega_3}$  define a Hurwitz polynomial.

### C. Optimization of Additional Criteria

As the final step, we now discuss how to exploit the 2-D actuation redundancy of the holocopter by exploiting vector  $\mathbf{z}$  in (16).

Being projected onto the null space of  $\mathbf{A}$ , vector  $\mathbf{z}$  does not produce actions interfering with the output-tracking objective and can thus be exploited to fulfill additional tasks. In our case, a first mandatory requirement is to keep  $\rho_A = 6$  at all times for avoiding singularities of the decoupling matrix  $\mathbf{A}$  in (16). As explained, this objective can be easily met by ensuring  $\mathbf{w} \neq \mathbf{0}$ . Likewise another important requirement is to minimize the norm of  $\mathbf{w}$  to reduce the energy consumption during flight since, for instance, the air drag torques  $\boldsymbol{\tau}_{\text{ext}_i}$  in (2) are always performing a dissipative work against  $w_i$ .

A possible cost function  $H(\mathbf{w})$  considering these two competing objectives is

$$H(\mathbf{w}) = \sum_{i=1}^4 h(w_i)$$

with

$$h(w_i) = \begin{cases} k_{h_1} \tan^2(\gamma_1 |w_i| + \gamma_2) & w_{\min} < |w_i| \leq w_{\text{rest}} \\ k_{h_2}(|w_i| - w_{\text{rest}})^2 & |w_i| > w_{\text{rest}} \end{cases} \quad (21)$$

$$\gamma_1 = \frac{\pi}{2(w_{\text{rest}} - w_{\min})}, \quad \gamma_2 = -\gamma_1 w_{\text{rest}}, \quad k_{h_1} > 0, \quad k_{h_2} > 0$$

suitable scalar gains. Here,  $w_{\min} > 0$  represents a minimum value for the propeller spinning velocities and  $w_{\text{rest}} > w_{\min}$  a suitable rest speed. Furthermore, functions  $h_i(w_i)$  are such that  $h_i(w_i) \rightarrow \infty$  if either  $|w_i| \rightarrow w_{\min}$  or  $|w_i| \rightarrow \infty$ , and have a unique minimum (with continuous derivative) at  $w_{\text{rest}}$ . For the placement of  $w_{\text{rest}}$ , in our implementation we chose

$$w_{\text{rest}} = \frac{mg}{4k_f} \quad (22)$$

that is, the (squared) spinning velocity needed by each propeller to hover.

An illustrative example for  $h_i(w_i)$  with  $w_{\min} = 126^2 \text{ [rad}^2/\text{s}^2]$  and  $w_{\text{rest}} = 450^2 \text{ [rad}^2/\text{s}^2]$  is shown in Fig. 6 (these values correspond to the ones used for the motor-propeller combination of our holocopter prototype).

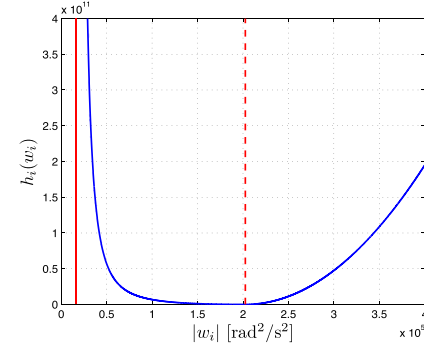


Fig. 6. Example of a function  $h_i(w_i)$  with  $w_{\min} = 126 \text{ [rad/s]}$  (solid red vertical line),  $w_{\text{rest}} = 450 \text{ [rad/s]}$  (dashed red vertical line). Note that  $h_i(w_i) \rightarrow \infty$  as  $|w_i| \rightarrow w_{\min}$  or  $|w_i| \rightarrow \infty$ , and that  $h_i(w_i)$  has a unique minimum at  $w_{\text{rest}}$  with continuous derivative.

Minimization of  $H(\mathbf{w})$ , compatibly with the output-tracking task, is then obtained by setting in (16)

$$\mathbf{z} = -k_H \begin{bmatrix} \nabla_{\mathbf{w}} H(\mathbf{w}) \\ \mathbf{0} \end{bmatrix} \quad (23)$$

where  $k_H > 0$  is the suitable step size. Note that, as a byproduct, this choice will also result in a beneficial velocity damping-like action on the states  $\mathbf{w}$  as, for example, described in [38]. We finally note that additional optimization actions could be embedded in vector  $\mathbf{z}$ , for instance by concurrently minimizing the second cost function  $H_{\alpha}(\boldsymbol{\alpha})$  representing constraints on the range of the tilting angles  $\boldsymbol{\alpha}$ .

### D. Final Considerations

We conclude the section by noting that the position/orientation feedback terms in (18)–(20) require a measurement of the holocopter:

- 1) position  $\mathbf{p}$  and orientation  ${}^W\mathbf{R}_B$ ;
- 2) linear velocity  $\dot{\mathbf{p}}$  and angular velocity  $\boldsymbol{\omega}_B$ ;
- 3) linear acceleration  $\ddot{\mathbf{p}}$  and angular acceleration  $\dot{\boldsymbol{\omega}}_B$ .

Availability of the quantities in items 1 and 2 is a standard requirement for any UAV flight control scheme (see also the next Section IV-B), whereas measurement of the linear/angular accelerations of item 3 can pose some challenges in real-world scenarios because of the typical high noise level of these signals when obtained from onboard sensors (e.g., accelerometers) or numerical differentiation of velocity-like quantities.

As an alternative, one can also exploit the holocopter model to evaluate the linear/angular acceleration  $(\ddot{\mathbf{p}}, \dot{\boldsymbol{\omega}}_B)$  in terms of sole velocity measurements (vector  $\mathbf{w}$ ) since, from (12), it follows that:

$$\begin{bmatrix} \ddot{\mathbf{p}} \\ \dot{\boldsymbol{\omega}}_B \end{bmatrix} = \mathbf{f} + \mathbf{J}_R \bar{\mathbf{J}}_{\alpha}(\boldsymbol{\alpha}) \mathbf{w}. \quad (24)$$

Obviously this possibility assumes a good knowledge of the model parameters and of the system state: the simulation and experimental results given in Sections V and VI are nevertheless conducted by relying on (24) for obtaining  $(\ddot{\mathbf{p}}, \dot{\boldsymbol{\omega}}_B)$ , and will thus confirm the appropriateness of this assumption for our setup.

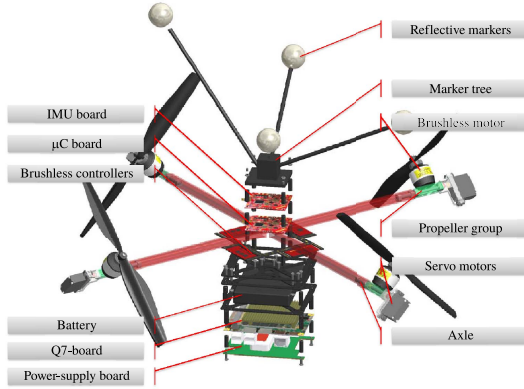


Fig. 7. Exploded view of the various components of the holocopter. All the important parts are properly labeled.

#### IV. HOLOCOPTER PROTOTYPE AND SYSTEM ARCHITECTURE

##### A. Prototype

For the first prototype, we opted for a very low-cost solution with all parts available off-the-shelf. The overall cost including all mechanical and electrical parts and actuators is below 1000 €. The mechanical main frame of the holocopter is based on the MikroKopter<sup>9</sup> module, including the propeller (EPP1045 CF) and the brushless propeller motors (Roxxy 2827-35). At the end of every arm of the holocopter body, a rigidly connected axle allows rotation of the propeller groups containing the propeller motor and the servo motor for the tilting actuation (Robbe S3150 Digital) (see Fig. 7). This has a maximum torque  $\tau_{\alpha_{\max}} = 0.37$  Nm and a maximum rotation speed  $\dot{\alpha}_{\max} = 4.1$  rad/s. The propeller group is designed to have its barycenter as close as possible to the axle, as assumed in the dynamical model developed in Section II.

Furthermore, two microcontroller boards are mounted on the top of the holocopter. The first contains the gyroscopes measuring  $\omega_B$ , and is also in charge of reading the tilting angles  $\alpha_i$  of the servo motors and the spinning velocities  $\bar{w}_i$  of the propellers. The second microcontroller board sends the desired spinning velocities  $\bar{w}_{\text{Des}_i}$  to the brushless controller and the desired angles  $\alpha_{\text{Des}_i}$  to the servo motors.

The trajectory tracking controller described in Section III is implemented in MATLAB/Simulink and, via the Real-Time Workshop toolbox, deployed and executed in real-time on an Intel Atom board (Quadmo747, from now on Q7-board) running the Linux Ubuntu10.10 real-time environment. The Q7-board is mounted below the battery and is equipped with a Wifi USB-dongle for communication. As only one RS-232 port (TTL level) is available on the Q7-board, the second microcontroller board is connected via USB-port and an USBToSerial converter. The Q7-board is powered by a battery, with the necessary voltage conversion and stabilization performed by a power-supply board containing a 12 V dc/dc power converter.

The nominal mass of the full holocopter is 1.32 kg. From a high-detail CAD model of the body and propeller groups, we

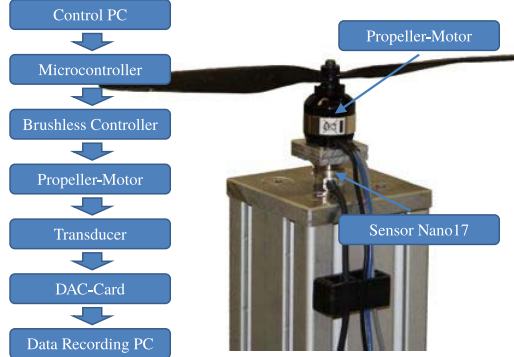


Fig. 8. Left: scheme of the measurement chain. Right: motor testbed including Propeller motor combination and Nano17 sensor mounted at a height of 0.45 m.

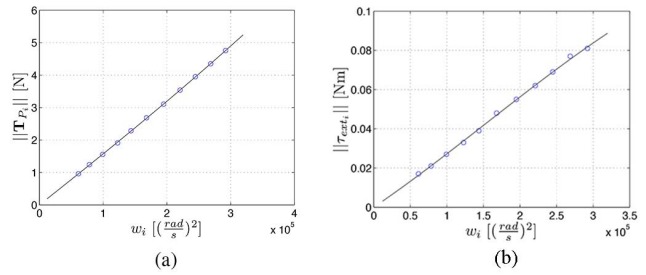


Fig. 9. (a) and (b) Dots: measured values of the thrust  $\|T_{P_i}\|$  and torque  $\|\tau_{ext_i}\|$  versus the signed squared spinning velocity  $w_i$ . Black lines: identified polynomial model (25) and (26).

also obtained the following inertia matrixes:

$$\mathbf{I}_{P_i} = \begin{bmatrix} 8.450e^{-5} & 0 & 0 \\ 0 & 8.450e^{-5} & 0 \\ 0 & 0 & 4.580e^{-5} \end{bmatrix} [\text{kg m}^2]$$

and

$$\mathbf{I}_B = \begin{bmatrix} 0.0154 & 0 & 0 \\ 0 & 0.0154 & 0 \\ 0 & 0 & 0.0263 \end{bmatrix} [\text{kg m}^2].$$

In the current setup, the servo motors are limited in their rotation by mechanical end stops in the range of  $-90^\circ < \alpha_i < 90^\circ$ . For our particular prototype, these limits translate into a maximum achievable rotation (in hover) of  $\approx \pm 55^\circ$  around the roll or pitch axes for the body frame  $B$  (this value was experimentally determined).

To obtain accurate values of  $k_f$  and  $k_m$  for our motor-propeller combination, we made use of a testbed equipped with a 6-dof torque/force sensor (Nano17-E, see Fig. 8) for identifying the mappings between the propeller spinning velocity and the generated thrust  $\|T_{P_i}\|$  and torque  $\|\tau_{ext_i}\|$  [see (2) and (3)]. This resulted in the following polynomial models (shown in Fig. 9):

$$\|T_{P_i}\| = 4.94e^{-18}|w_i|^3 + 9.62e^{-13}|w_i|^2 + 1.56e^{-5}|w_i| \quad (25)$$

and

$$\|\tau_{ext_i}\| = -5.41e^{-19}|w_i|^3 + 2.50e^{-13}|w_i|^2 - 2.53e^{-7}|w_i| \quad (26)$$

<sup>9</sup><http://www.mikrokopter.de>

where  $w_i = \bar{w}_i |\bar{w}_i|$  is the signed square of the propeller spinning velocity as previously explained. The controller (16) was then implemented by directly exploiting the mappings (25) and (26) for obtaining  $(\|\mathbf{T}_{P_i}\|, \|\boldsymbol{\tau}_{\text{ext}_i}\|)$ , and by replacing

$$k_f = \frac{\partial \|\mathbf{T}_{P_i}\|}{\partial w_i} \Big|_{w_i} \quad \text{and} \quad k_m = \frac{\partial \|\boldsymbol{\tau}_{\text{ext}_i}\|}{\partial w_i} \Big|_{w_i}$$

both evaluated upon the measured  $w_i$ .

### B. System Architecture

The Q7-board runs a GNU-Linux Ubuntu 10.10 real-time OS and executes the MATLAB-generated code. The controller runs at 500 Hz and takes as inputs: 1) the desired trajectory  $(\mathbf{p}_d(t), \mathbf{R}_d(t))$  and needed derivatives  $(\dot{\mathbf{p}}_d(t), \ddot{\mathbf{p}}_d(t), \ddot{\mathbf{p}}_d(t))$  and  $(\boldsymbol{\omega}_d(t), \dot{\boldsymbol{\omega}}_d(t), \ddot{\boldsymbol{\omega}}_d(t))$ ; 2) the current position/orientation of the holocopter  $(\mathbf{p}, {}^W\mathbf{R}_B)$  and its linear/angular velocity  $(\dot{\mathbf{p}}, \boldsymbol{\omega}_B)$ ; 3) the spinning velocities of the propellers  $w_i$ ; and 4) the tilting angles  $\alpha_i$ .

The position  $\mathbf{p}$  and orientation  ${}^W\mathbf{R}_B$  of the holocopter are directly obtained from an external motion capture system<sup>10</sup> (MoCap) at 200 Hz. A marker tree consisting of five infrared markers is mounted on top of the holocopter for this purpose. Knowing  $\mathbf{p}$ , the linear velocity  $\dot{\mathbf{p}}$  is then obtained via numerical differentiation, while the angular velocity  $\boldsymbol{\omega}_B$  is measured by the onboard Inertial Measurement Unit (IMU) (three ADXRS610 gyroscopes).

Because of performance reasons (bottleneck in serial communication), the sending of the desired motor speeds and tilting angles, and the reading of the IMU-data, of the actual spinning velocities, and of tilting angles is split among two communication channels and two microcontrollers (called, from now on,  $\mu$ C-Board and IMU-Board). The desired motor spinning velocities  $w_{\text{Des}_i}$  are sent from the Q7-board to the  $\mu$ C-Board via a serial connection at the frequency of 250 Hz and 8 b resolution, and from the  $\mu$ C-Board to the brushless controllers via I<sup>2</sup>C-bus at again 250 Hz. In the same manner, the actual spinning velocities  $w_i$  of the four propellers can be read back at a frequency of 250 Hz and a resolution of 8 b. The brushless controllers implement a PID-controller for regulating the spinning velocity. The desired tilting angles  $\alpha_{\text{Des}_i}$  are sent from the Q7-board to the  $\mu$ C-Board via the same serial connection at a frequency of 55 Hz and 10 b resolution, and from the  $\mu$ C-Board to the servo motors via PWM (signal length 15 ms). We note that the trajectory tracking controller described in Section III assumes availability of the tilting velocities  $w_{\alpha_i}$  as inputs [see (16)], whereas the current architecture only allows for sending desired angles commands  $\alpha_{\text{Des}_i}(t)$ . This is addressed by numerically integrating over time the controller commands  $w_{\alpha_i}$ , that is, by implementing

$$\alpha_{\text{Des}_i}(t) = \int_{t_0}^t w_{\alpha_i}(\tau) d\tau + \alpha_i(t_0) \quad (27)$$

where  $\alpha_i(t_0)$  is the  $i$ th measured tilting angle at the beginning of motion.<sup>11</sup>

<sup>10</sup><http://www.vicon.com/products/bonita.html>

<sup>11</sup>We note that, in order to avoid possible numerical drifts, one could also exploit the measured  $\alpha_i(t)$  for resetting (27) when needed.

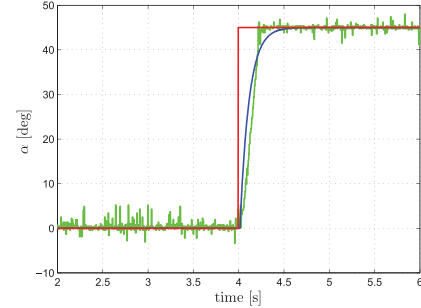


Fig. 10. Modeling of the servo motor. Behavior of the real servo motor (green) and the model (blue) following a step input (red) of  $45^\circ$  after compensating for the (known) transport delay  $T = 18$  ms.

The IMU-Board reads the current angles  $\alpha_i$  of the propeller groups  $P_i$  by a direct connection between the servo motor potentiometer and the A/D-converter of the microcontroller (10 b resolution at 250 Hz). It also retrieves the current spinning velocities  $\bar{w}_i$  of the propellers via the I<sup>2</sup>C-Bus (8 b resolution and 250 Hz). The gyro data are read at 250 Hz and converted with 10 b resolution. Finally, the values of  $\alpha_i$ ,  $\bar{w}_i$ , and the gyro data are transmitted from the IMU-Board to the Q7-board via the RS232-port at 250 Hz. All values of the controller can be monitored on a remote Windows PC which mirrors the running controller in real-time using the MATLAB/simulink external mode. This simplifies the development as most of the gains and settings can be changed online during flight tests.

The communication architecture for the tilting angles  $\alpha_{\text{Des}_i}$  (in particular, the PWM modulation) unfortunately introduces a nonnegligible roundtrip delay of about 18 ms from sent commands to read values. We experimentally found this delay to significantly degrade the closed-loop performance of the controller, and therefore propose in Section IV-C a simple prediction scheme for mitigating its adverse effects.

### C. Coping With the Nonidealities of the Servo Motors

The  $i$ th servo motor for the tilting angles can be approximately modeled as a linear transfer function  $G(s)$  with, in series, a transport delay of  $T = 18$  ms, that is, as the delayed linear system  $\alpha_i(s) = G(s)e^{-Ts}\alpha_{\text{Des}_i}(s)$ . A model of the undelayed  $G(s)$  was experimentally obtained by measuring the step response of the servo motors while having the propellers spinning at  $\bar{w}_i = 450$  rad/s (the velocity corresponding to hovering), and by compensating offline for the known delay  $T$  (see Fig. 10). This resulted into the estimated transfer function

$$G_{\text{est}}(s) = \frac{0.4s + 6}{0.06s^2 + s + 6}. \quad (28)$$

The performance degradation of the cartesian trajectory controller (16)–(23) can then be due to two main effects, namely presence of the transport delay  $T$  and slow dynamic response of  $G_{\text{est}}(s)$  to fast changing inputs. To mitigate these shortcomings, we resorted to the following simple strategy (see Fig. 11); instead of feeding back the measured (i.e., delayed) angles  $\alpha_i$  to the cartesian controller (16)–(23), we replaced them with the (undelayed) desired angles  $\alpha_{\text{Des}_i}$  from (27). In parallel, we aimed at improving the servo

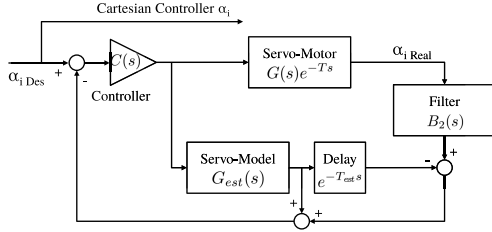


Fig. 11. Scheme of the Smith predictor for  $\alpha_i$  including the controller  $C(s)$ , the servo motor  $G(s)e^{-Ts}$ , the model of the servo motor  $G_{est}(s)e^{-T_{est}s}$ , and the Butterworth filter  $B_2(s)$ .

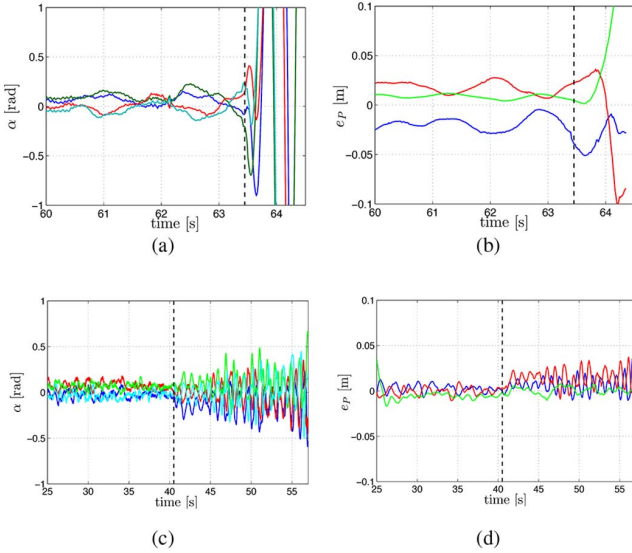


Fig. 12. Results of the experiments assessing the effectiveness of the scheme in Fig. 11. In all the plots, the vertical dashed black line indicates the time  $t_{off}$  after which the scheme is switched off. (a) Behavior of the tilting angles  $\alpha(t)$  during case I. (b) Position-tracking error  $e_P(t)$  during case I. (c) Behavior of tilting angles  $\alpha(t)$  during case II. (d) Position-tracking error  $e_P(t)$  during case II. Note how in both cases the holocopter becomes unstable for  $t \geq t_{off}$ , thus confirming the validity of the scheme in Fig. 11 in coping with the nonidealities of the employed servo motors.

motor performance (i.e., making  $G_{est}(s)$  more responsive) by resorting to a Smith predictor scheme [39]. In fact, as well known from classical control theory, the Smith predictor is an effective tool for coping with known delays affecting known stable linear systems. In our case, an additional outer PID controller  $C(s)$  plugged into the Smith predictor loop (as shown in Fig. 11), allowed to improve the rising time of the servo controller. Finally, because we found the measured angles  $\alpha_i$  to be affected by significant noise, we filtered their readings with the second-order Butterworth filter with a cutoff frequency of 20 Hz. The location of this cutoff frequency was experimentally determined by analyzing offline the power spectrum of the angles  $\alpha_i$  recorded during a hovering flight of 40 s.

As experimental proof of the effectiveness of the aforementioned strategy in coping with the nonidealities of the holocopter actuation system, we ran the following two illustrative experiments involving a simple hovering on the spot task. In both experiments, the scheme shown in Fig. 11 was activated for an initial period  $0 \leq t \leq t_{off}$  after which the scheme was instead switched off: for  $t \geq t_{off}$  the trajectory

TABLE III  
MEAN SPINNING VELOCITY  $\bar{w}$  OF THE FOUR PROPELLERS FOR DIFFERENT HOVERING ORIENTATIONS

Pose	Mean spinning velocity $Avg(\bar{w})$
$\theta = 0 \text{ rad}, \phi = 0 \text{ rad}, \psi = 0 \text{ rad}$	$450 \frac{\text{rad}}{\text{s}}$
$\theta = \frac{\pi}{4} \text{ rad}, \phi = 0 \text{ rad}, \psi = 0 \text{ rad}$	$504 \frac{\text{rad}}{\text{s}}$
$\theta = \frac{\pi}{2} \text{ rad}, \phi = 0 \text{ rad}, \psi = 0 \text{ rad}$	$465 \frac{\text{rad}}{\text{s}}$
$\theta = \frac{\pi}{2} \text{ rad}, \phi = 0 \text{ rad}, \psi = \frac{\pi}{4} \text{ rad}$	$530 \frac{\text{rad}}{\text{s}}$

controller was then fed back with the measured (and thus delayed) angles  $\alpha_i(t)$  (case I), and with the desired angles  $\alpha_{Des_i}(t)$  (case II).

The results are shown in Fig. 12(a)–(d). We first note how, in both cases, the hovering task is correctly realized during  $0 \leq t \leq t_{off}$ , that is, when employing the scheme shown in Fig. 11. Then, in case I the holocopter becomes unstable almost instantaneously for  $t > t_{off}$ , while in case II the servo motors start to slowly oscillate to then reach practical instability at about  $t > t_{off} + 15 \text{ s}$ . These results allow us to then conclude the ability of the proposed strategy to cope with the shortcomings of the holocopter actuation system.

#### D. Energetic Efficiency of the Holocopter in Hovering

As a final consideration, we briefly discuss the energetic efficiency of the holocopter in a hovering condition. Indeed, we note that the holocopter energetic efficiency for arbitrary hovering orientations can be less than in the (standard) horizontal case ( $\phi = 0, \theta = 0$ ), and also despite the optimization action (23). This is due to the adopted mechanical design which allows each propeller to only rotate about one tilting angle (angles  $\alpha_i$ ): therefore, there will exist hovering orientations at which the thrust vectors  $T_{P_i}$  cannot be aligned against gravity, with thus some of the thrust lost in internal forces. This reduced efficiency cannot be completely avoided with the adopted design, but only partially mitigated via optimization actions such as (23). In this sense, Table III gives an illustration of the energetic efficiency of our prototype (in terms of the mean spinning velocity of the four propellers) obtained at several hovering conditions (including the horizontal one).

## V. SIMULATION RESULTS

We now report some simulation results aimed at validating the proposed control design. We first consider in Section V-A an ideal case in which controller (16) is tested on the complete holocopter dynamical model described in Section II, that is, by including all the inertial/gyroscopic effects neglected at the control design stage. These results are meant to illustrate the flying performance of the holocopter in ideal conditions, that is, when not considering all the limitations and nonidealities affecting the real prototype as in Section IV-B.

Subsequently, we present in Section V-B an additional set of realistic simulations that explicitly include the prototype main nonidealities (data-exchange rates, control frequencies, and actuation delays). In these simulations, the controller (16) is also complemented with the prediction scheme described in Section IV-C so as to replicate, as much as possible, the control

architecture of the real prototype. The results are intended to show the robustness of the adopted control approach as the holocopter is still able to execute complex trajectories although with a poorer flight performance compared with the ideal case (as expected). Furthermore, a comparison between both cases clearly shows the margin left for improving the actuation system of our prototype in its second generation (see Section VII).

#### A. Ideal Simulations

The aim of the following simulations is twofold: on one side, we want to highlight the tracking capabilities of the proposed controller and the beneficial action of the null-space term (19) in avoiding singularities for the decoupling matrix  $\mathbf{A}(\boldsymbol{\alpha}, \boldsymbol{\omega})$ . On the other side, we also want to show the robustness of the controller against all the inertial/gyroscopic effects neglected at the control design stage but included in the quadrotor dynamic model (1–5).

1) *Rotation on Spot*: In this first simulation, we tested a simple trajectory involving a rotation of  $\pi$  rad on the spot along the  $\mathbf{Y}_B$  axis.<sup>12</sup> The initial conditions were set to  $\mathbf{p}(t_0) = \mathbf{0}$ ,  $\dot{\mathbf{p}}(t_0) = \mathbf{0}$ ,  $\mathbf{R}(t_0) = \mathbf{I}_3$ ,  $\boldsymbol{\omega}_B(t_0) = \mathbf{0}$ ,  $\boldsymbol{\alpha}(t_0) = \mathbf{0}$ ,  $\dot{\boldsymbol{\alpha}}(t_0) = \mathbf{0}$ , and  $\mathbf{w}(t_0) = w_{\text{rest}}$ . The desired trajectory was chosen as  $\mathbf{p}_d(t) \equiv 0$  and  $\mathbf{R}_d(t) = \mathbf{R}_X(\phi(t))$  with  $\phi(t)$  following a smooth profile with maximum velocity  $\dot{\phi}_{\max} = 0.49$  rad/s and maximum acceleration  $\ddot{\phi}_{\max} = 0.16$  rad/s<sup>2</sup>. The trajectory was executed twice by: 1) including and 2) not including the null-space term  $\mathbf{z}$  (23) into (16) ( $k_H = 1$  or  $k_H = 0$ ). The gains in (18)–(20) were set to  $\mathbf{K}_{p_1} = 28.5\mathbf{I}_3$ ,  $\mathbf{K}_{p_2} = 271\mathbf{I}_3$ ,  $\mathbf{K}_{p_3} = 857\mathbf{I}_3$  and  $\mathbf{K}_{\omega_1} = 45\mathbf{I}_3$ ,  $\mathbf{K}_{\omega_2} = 675\mathbf{I}_3$ , and  $\mathbf{K}_{\omega_3} = 3375\mathbf{I}_3$ .

Fig. 13(a)–(f) shows the results of the simulation in these two cases. In particular, Fig. 13(a) shows the superimposition of  $H(\mathbf{w})$  when including  $\mathbf{z}$  [red dashed line, case (i)] and not including  $\mathbf{z}$  [blue solid line, case (ii)]. It is clear that, in the first case,  $H(\mathbf{w})$  attains a lower value over time thanks to the optimization action in (23). As a consequence, this results in a lower value for  $\|\mathbf{w}\|$  over time as shown in Fig. 13(b) (same color pattern), showing that the given task (rotation on the spot) can be realized in a more energy-efficient way when properly shaping the cost function  $H(\mathbf{w})$ . Note that, as a byproduct, the better performance of case (i) comes at the expense of a more complex reorientation of the propeller groups during the motion. This is shown in Fig. 13(c) and (d) which report the behavior of the four tilt angles  $\alpha_i$  in cases (i) (left) and (ii) (right): compared with Fig. 13(d), note the rotation of two propellers starting from  $t \approx 25.8$  [s] in Fig. 13(c).

Finally, Fig. 13(e) and (f) shows, for case (i) only, the position-tracking error  $\mathbf{e}_P(t) = \mathbf{p}_d(t) - \mathbf{p}(t)$  and orientation-tracking error  $\mathbf{e}_R(t)$  as defined in (19). Despite the fast reorientation of two propellers shown in Fig. 13(c), the tracking errors stay small (note the scales) and eventually converge to zero as the desired trajectory comes to a full stop. Also, as one would expect, the largest peaks for the errors

<sup>12</sup>This upside-down flip motion would be clearly unfeasible for a standard quadrotor. It is (unfortunately) also unfeasible for the current experimental prototype because of the mechanical end stops in the propeller tilting actuation (see Section IV-A).

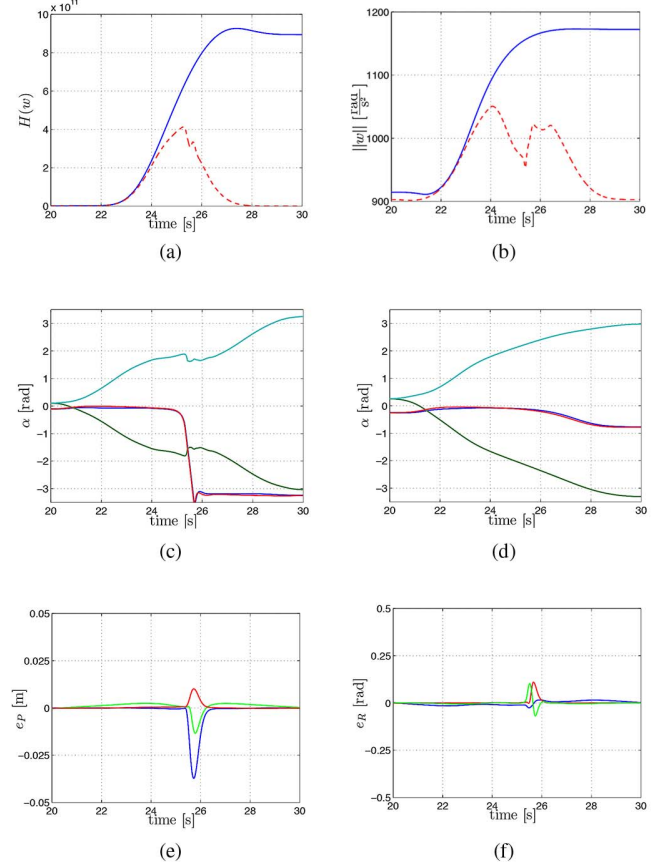


Fig. 13. Results of the first ideal simulation with (i) and without (ii) exploiting the null-space term (23). (a) Behavior of  $H(\mathbf{w})$  for cases (i) (red dashed line) and (ii) (blue solid line). (b) Behavior of  $\|\mathbf{w}\|$  for cases (i) (red dashed line) and (ii) (blue solid line). (c) and (d) Behavior of the tilt angles  $\alpha$  for cases (i) (left) and (ii) (right). (e) and (f) Behavior of the position-/orientation-tracking errors ( $\mathbf{e}_P$ ,  $\mathbf{e}_R$ ) for case (ii).

$\mathbf{e}_P(t)$  and  $\mathbf{e}_R(t)$  occur at about  $t \approx 25.8$  [s], that is, during the fast reorientation of the two propellers because of the internal gyroscopic effects treated as external disturbances by the controller.

These results then provide a first confirmation of the validity of our assumptions in Section III, that is, robustness of the controller with respect to the gyroscopic/inertial effect due to the internal relative motion of the different bodies composing the quadrotor. For the reader's convenience, we also report in Fig. 14(a) and (b) a series of snapshots illustrating the quadrotor motion in these two cases [note the very different final configuration of the propeller group in cases (i) and (ii)].

2) *Eight-Shape Trajectory*: In this second simulation, the holocopter task is to track a planar eight-shape trajectory  $\mathbf{p}_d(t)$  while, at the same time, performing a sinusoidal rotation around the  $\mathbf{Y}_B$  axis. The chosen desired trajectory  $\mathbf{p}_d(t)$  is a horizontal eight-shape with size of 1.0 m by 1.4 m and lying at a height of  $z = 1.0$  m from ground, that is

$$\mathbf{p}_d(t) = \begin{bmatrix} 0.5 \sin(0.135t) \\ 0.7 \sin(0.27t) \\ 1 \end{bmatrix} [\text{m}] \quad (29)$$

[see Fig. 15(a)].

As for the rotation about  $\mathbf{Y}_B$ , Fig. 15(b) shows the chosen profile for the pitch angle  $\theta(t)$ . The main quantities of interest

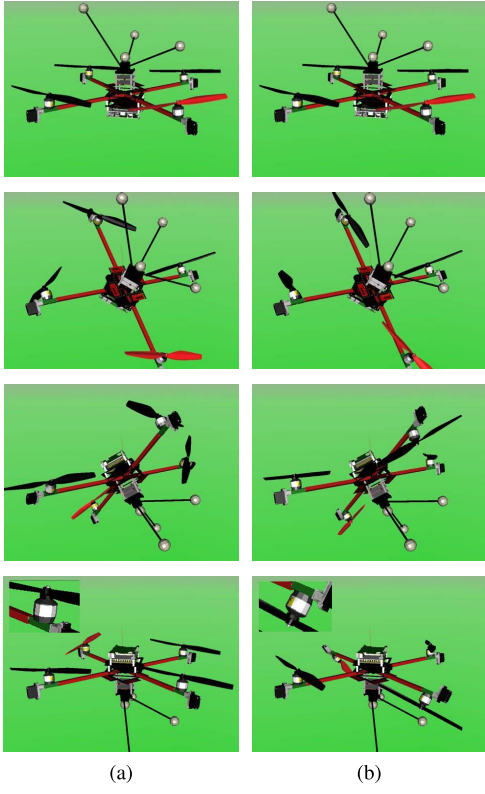


Fig. 14. Results of the first ideal simulation. Left column: holocopter motion while minimizing  $H(\mathbf{w})$  [case (i)]. Right column: holocopter motion without minimizing  $H(\mathbf{w})$  [case (ii)]. Note the large reorientation of the propeller groups in case (i) which, thanks to the action of the optimization term (23), end up in a full upright position (minimum energy consumption) with respect to case (ii).

are in this case:

- 1) maximum speed along the trajectory:  $v_{\max} = 0.20 \text{ m/s}$ ;
- 2) maximum acceleration along the trajectory:  $a_{\max} = 0.05 \text{ m/s}^2$ ;
- 3) amplitude of the sinusoidal rotation:  $\theta_{\max} = 0.17 \text{ rad}$ ;
- 4) maximum rotational velocity:  $\dot{\theta}_{\max} = 0.05 \text{ rad/s}$ ;
- 5) maximum rotational acceleration:  $\ddot{\theta}_{\max} = 0.02 \text{ rad/s}^2$ .

Fig. 16(a) and (b) shows the position- and orientation-tracking errors ( $e_P(t)$ ,  $e_R(t)$ ) while performing the task, with maximum values of  $e_{P\max} \simeq 0.28 \text{ mm}$  and  $e_{R\max} \simeq 0.0035 \text{ rad}$ . Again, these errors can be ascribed to the unmodeled internal gyroscopic and inertial forces caused by the propeller group rotations with respect to the body frame. The behavior of  $\alpha(t)$  is also shown in Fig. 16(c). The results of the simulation demonstrate again the tracking abilities of the proposed controller as the position and orientation errors keep very small values while following this more complex trajectory.

### B. Realistic Simulations

As explained, the realistic simulations of this section have been obtained by including in the holocopter model all the nonidealities of our real prototype, in particular by replicating the various signal and control frequencies (e.g., motion capture frequency at 200 Hz, servo motor frequency at 70 Hz) and delays (e.g., servo motor delay of 18 ms). In addition, we also

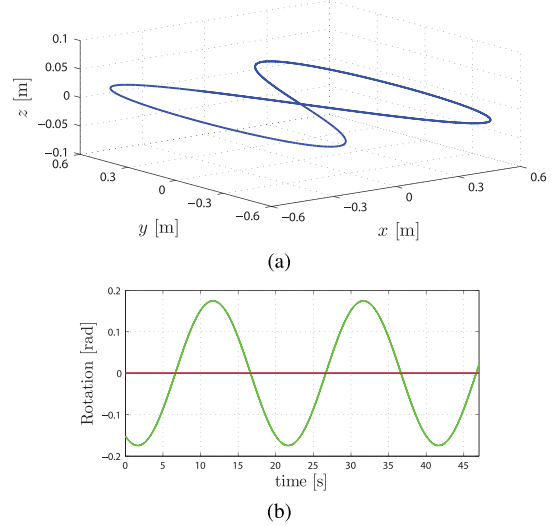


Fig. 15. Results of the second ideal simulation. (a) Desired eight-shape trajectory. (b) Desired sinusoidal orientation over time, red line indicates desired pitch angle  $\theta$ .

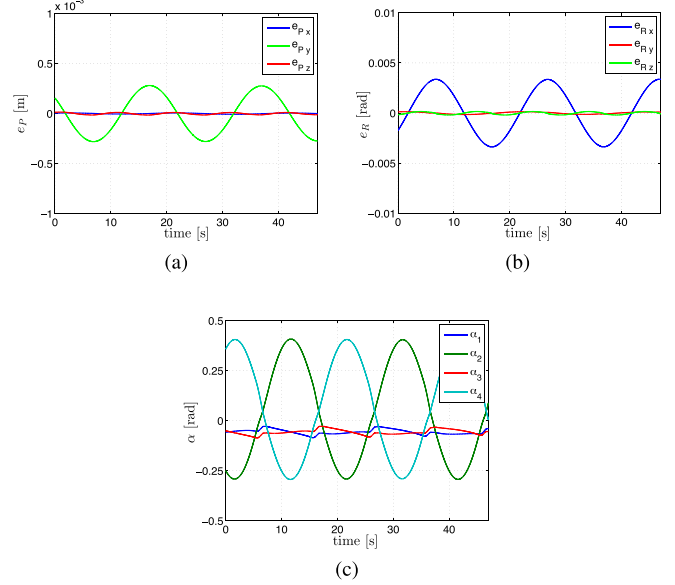


Fig. 16. Results of the second ideal simulation. (a) Position-tracking error  $e_P(t)$ . (b) Orientation-tracking error  $e_R(t)$ . (c) Behavior of the tilt angles  $\alpha(t)$  while tracking the trajectory.

considered the noise of onboard sensor readings (gyroscopes, accelerometers, and measurement of angles  $\alpha$ ), of the actuators (servo and propeller motors), and of the motion capture system by either obtaining the noise characteristics from data sheets, or via a preliminary off-line identification. Finally, the prediction scheme described in Section IV-C was implemented in the control loop.

Despite assessing the effects of these nonidealities on the overall flight performance, the results of this section are also helpful for saving development time as they allow a pretuning of the various control gains for the deployment on the real prototype, and the identification of the most influential parameters to be optimized in view of the second-generation prototype.

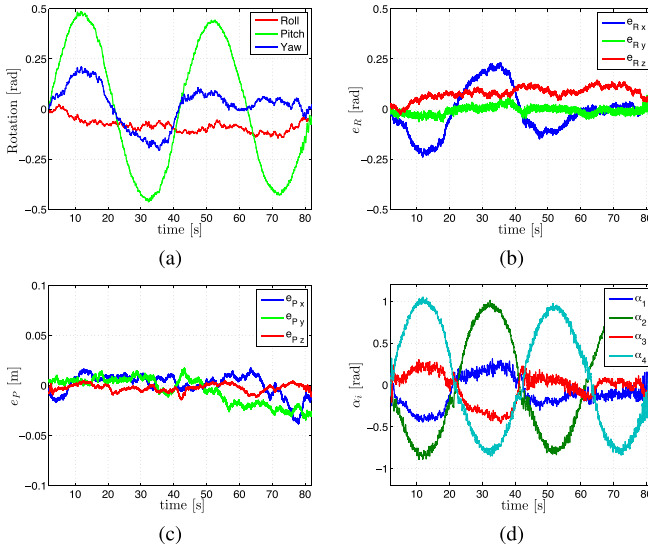


Fig. 17. Results of the first realistic simulation. Rotation on the spot around the  $Y_B$ -axis. (a) Orientation of the main body B. (b) and (c) Orientation-tracking error  $e_R(t)$  and position-tracking error  $e_P(t)$ . (d) Behavior of the tilting angles  $\alpha(t)$ .

*1) Rotation on Spot:* Because of the limited range of the tilting angles  $\alpha$  in the real prototype, it is not possible to perform a full rotation on the spot as in the previous ideal case explained in Section V-A 1. Therefore, we opted for a (more feasible) sinusoidal rotation around the  $Y_B$ -axis (pitch), that is, with  $\mathbf{R}_d(t) = \mathbf{R}_Y(\theta(t))$  with  $\theta_{\max} = 0.436$  rad and  $\dot{\theta}_{\max} = 0.07$  rad/s. The initial conditions were set to hovering ( $\mathbf{p}(t_0) = \mathbf{0}$ ,  $\dot{\mathbf{p}}(t_0) = \mathbf{0}$ ,  $\mathbf{R}(t_0) = \mathbf{I}_3$ ,  $\boldsymbol{\omega}_B(t_0) = \mathbf{0}$ ,  $\boldsymbol{\alpha}(t_0) = \mathbf{0}$ , and  $\mathbf{w}(t_0) = w_{\text{rest}}$ ), and the controller gains were chosen as  $\mathbf{K}_{p_1} = 30\mathbf{I}_3$ ,  $\mathbf{K}_{\omega_1} = 55.5\mathbf{I}_3$ ,  $\mathbf{K}_{p_2} = 300\mathbf{I}_3$ ,  $\mathbf{K}_{\omega_2} = 1027\mathbf{I}_3$ ,  $\mathbf{K}_{p_3} = 1000\mathbf{I}_3$ ,  $\mathbf{K}_{\omega_3} = 6331\mathbf{I}_3$ .

The results are shown in Fig. 17(a)–(d); Fig. 17(a) shows the behavior of the quadrotor orientation during flight (blue: roll, green: pitch, red: yaw) and Fig. 17(b) the behavior of the orientation error  $e_R(t)$ . The maximum rotation errors are 0.240 rad (roll), 0.079 rad (pitch), and 0.144 rad (yaw). Fig. 17(c) shows the behavior of the position-tracking error  $e_P(t)$  characterized by a mean value  $\text{avg}(\|e_P(t)\|) \approx 1.6$  cm and a maximum value  $\text{max}(\|e_P(t)\|) \approx 4.4$  cm. Finally, Fig. 17(d) shows the behavior of the tilting angles  $\alpha(t)$  over time.

Therefore, despite the (expected) worse overall performance with respect to the ideal case, in this realistic case the holocopter is still able to fulfill the assigned motion task with a good enough accuracy.

*2) Eight-Shape Trajectory:* In this simulation, we considered the same eight-shape trajectory illustrated in Section V-A 2. Fig. 18(a) and (b) shows the behavior of the position and orientation error vectors ( $\mathbf{e}_P(t)$ ,  $\mathbf{e}_R(t)$ ) over time. The average position-tracking error results about 0.034 m with a maximum of 0.050 m. The maximum rotation errors are 0.097 rad (roll), 0.061 rad (pitch), and 0.039 rad (yaw). Finally, Fig. 18(c) shows the behavior of the tilting angles  $\alpha_i(t)$  while following the trajectory.

It is interesting to compare these results with those of the ideal simulation described in Section V-A.2 [Fig. 16(a)–(c)].

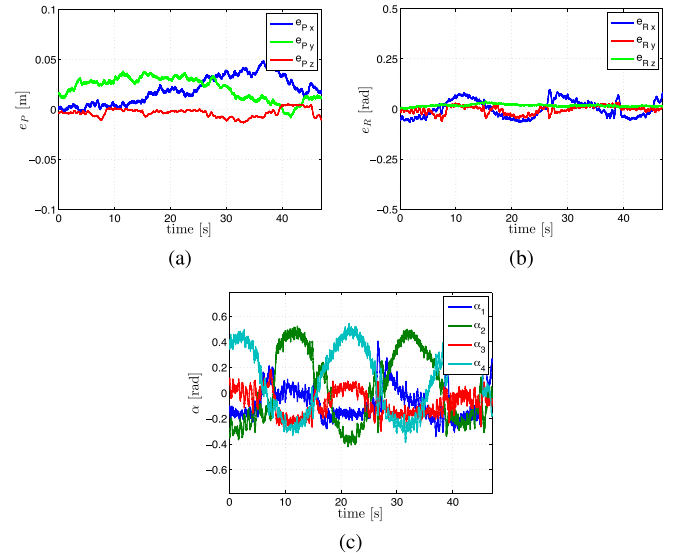


Fig. 18. Results of the second realistic simulation. (a) Position-tracking error  $e_P(t)$ . (b) Orientation-tracking error  $e_R(t)$ . (c) Behavior of the tilting angles  $\alpha_i(t)$ .

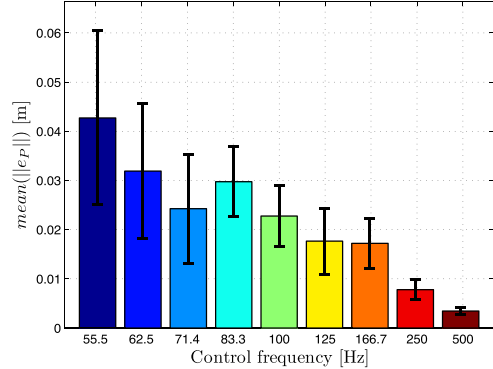


Fig. 19. Mean position error  $\text{avg}(\|e_P\|)$  and standard deviation of the position error  $\text{stdev}(\|e_P\|)$  for different PWM control frequencies of the servo motors while following the eight-shape trajectory reported in Section V-A 2.

again, the overall tracking performance results degraded with respect to the ideal case, although the holocopter can still realize the task with a sufficient accuracy. Also, note how the angles  $\alpha_i(t)$  shown in Fig. 18(c) follow essentially the same behavior as those of the ideal case shown in Fig. 16(c) despite the higher noise level present in the system.

*3) Effect of Servo Control Frequency:* As previously stated, the low control rate and the delayed response of the employed servo motors are expected to be the main cause of the flight performance degradation in the realistic case (and, of course, in the real prototype). The servo motors are controlled via a pulse-width-modulated (PWM) signal with a signal length of 14 ms and a control frequency of 55 Hz. To assess the effects of these parameters, we ran several instances of the previous realistic simulation described in Section V-B.2 by employing increasing control frequencies and correspondingly decreasing delays for the servo motor PWM while keeping all the other parameters (e.g., control gains) constant.

As flight performance measure, we considered the mean position error  $\text{avg}(\|e_P(t)\|)$  and the standard deviation of the position error  $\text{stdev}(\|e_P(t)\|)$  during the trajectory. Fig. 19 shows the results: with an increasing control frequency,

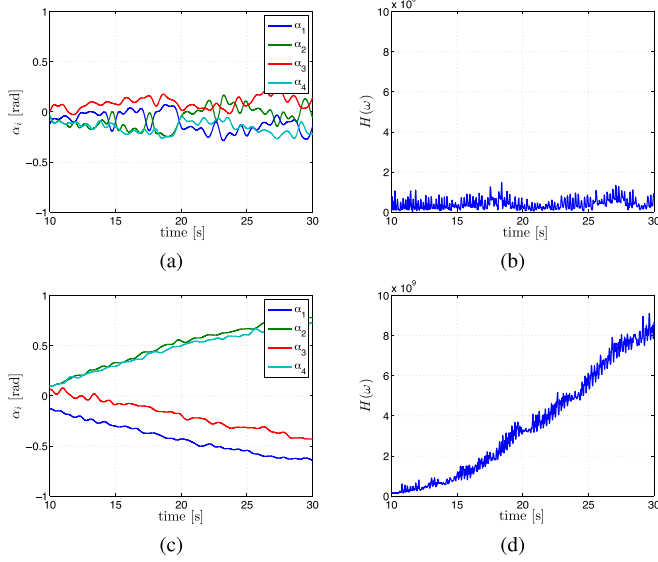


Fig. 20. First experiment. Results for hovering on the spot with (i) and without (ii) including the null-space term (23). (a)  $\alpha_i$  for case (i) while hovering. (b)  $H(\mathbf{w})$  for case (i) while hovering. (c)  $\alpha_i$  for case (ii) while hovering. (d)  $H(\mathbf{w})$  for case (ii) while hovering.

the mean position error and the standard deviation are clearly decreasing from, for example,  $\text{avg}(\|\mathbf{e}_P\|)_{55 \text{ Hz}} = 0.042 \text{ m}$  to  $\text{avg}(\|\mathbf{e}_P\|)_{500 \text{ Hz}} = 0.003 \text{ m}$ , thus approaching the performance of the ideal case.

## VI. EXPERIMENTAL RESULTS

In this last section, we finally present results from three experiments conducted with the holocopter prototype. The first experiment is a hovering task meant to show the overall performance in the simplest scenario, and also to highlight again the importance of having included the null-space optimization term (23) in the control strategy. The other two experiments involve instead the more complex trajectories illustrated in Sections V-B.1 and V-B.2. Finally we encourage the reader to watch the video clip attached to this paper where several holocopter maneuvers are shown along with additional details on the employed prototype.

### A. Hovering on the Spot

In the first experiment, following what was done in the ideal case explained in Section V-A.1, we show the importance of having included the minimization of the cost function  $H(\mathbf{w})$  in the proposed controller. To this end, we report the results of a simple hovering on the spot by (i) including and (ii) not including the null-space optimization term (23). The quadrotor starts from the initial state of  $\mathbf{p}(t_0) = \mathbf{0}$ ,  $\dot{\mathbf{p}}(t_0) = \mathbf{0}$ ,  $\mathbf{R}(t_0) = \mathbf{I}_3$ ,  $\boldsymbol{\omega}_B(t_0) = \mathbf{0}$ ,  $\boldsymbol{\alpha}(t_0) = \mathbf{0}$ , and  $\mathbf{w}(t_0) = w_{\text{rest}}$ , and is commanded to stay still while maintaining the desired attitude  $\mathbf{R}_d = \mathbf{I}_3$ . The gains in (18) and (20) were set to  $\mathbf{K}_{p1} = 30\mathbf{I}_3$ ,  $\mathbf{K}_{\omega_1} = 55.5\mathbf{I}_3$ ,  $\mathbf{K}_{p2} = 300\mathbf{I}_3$ ,  $\mathbf{K}_{\omega_2} = 1027\mathbf{I}_3$ ,  $\mathbf{K}_{p3} = 1000\mathbf{I}_3$ ,  $\mathbf{K}_{\omega_3} = 6331\mathbf{I}_3$  (these values were experimentally tuned).

Fig. 20(a) and (b) shows the results for case (i): the angles  $\alpha_i$  stay close to 0 rad over time, as expected for such a hovering

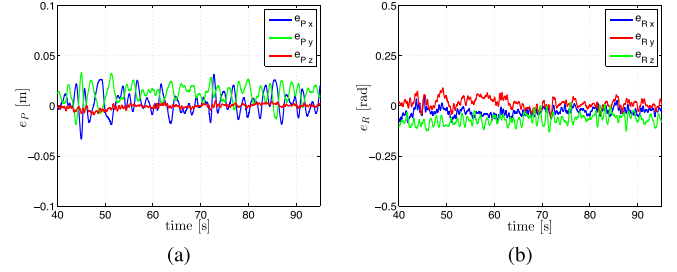


Fig. 21. First experiment. Tracking error while hovering (a) position-tracking error  $\mathbf{e}_P(t)$  and (b) orientation-tracking error  $\mathbf{e}_R(t)$ .

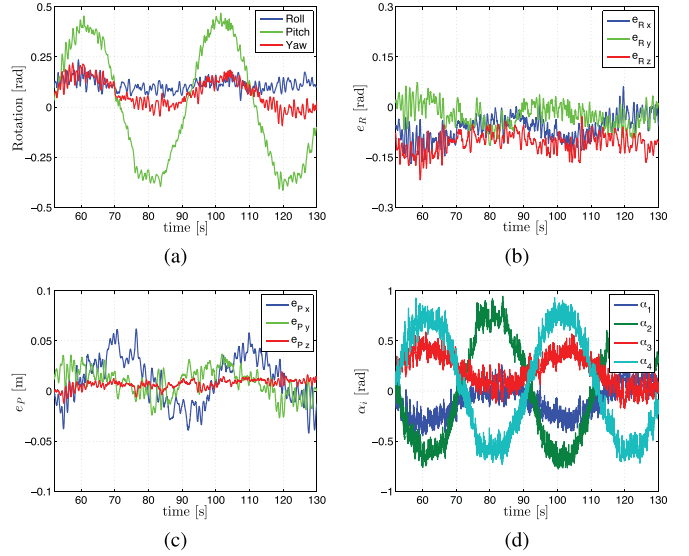


Fig. 22. Second experiment. Rotation on the spot around the  $\mathbf{Y}_B$ -axis. (a) Orientation of the main body B. (b) and (c) Orientation error vector  $\mathbf{e}_R(t)$  and position error vector  $\mathbf{e}_P(t)$ . (d) Behavior of the tilting angles  $\alpha_i$ .

maneuver, and  $H(\mathbf{w})$  keeps a constant and low value as the propellers spin with a speed close to the allowed minimum. In case (ii), however, the situation looks completely different: the lack of any minimization action on  $H(\mathbf{w})$ , coupled with the presence of noise and nonidealities, makes the angles  $\alpha_i$  to eventually diverge over time from their (expected) vertical direction and, accordingly, the value of  $H(\mathbf{w})$  to increase as the propellers need to accelerate to keep the quadrotor still in place [Fig. 20(c) and (d)].

Finally, Fig. 21(a) and (b) shows the position error  $\mathbf{e}_P(t)$  and orientation error  $\mathbf{e}_R(t)$  during the experiment. The average position-tracking error is about 0.017 m with a maximum of 0.047 m. The maximum rotation errors are 0.082 rad (roll), 0.131 rad (pitch), and 0.089 rad (yaw).

### B. Rotation on the Spot

In this second experiment, we replicate the realistic simulation case explained in Section V-B.1 by commanding the holocopter to follow a given orientation profile  $\mathbf{R}_d(t)$  while remaining still in space. The initial conditions, control gains, and trajectory parameters are the same as those reported in Section V-B.1.

Fig. 22(a)–(d) shows the results of the flight: in particular, Fig. 18(a) reports the quadrotor orientation during

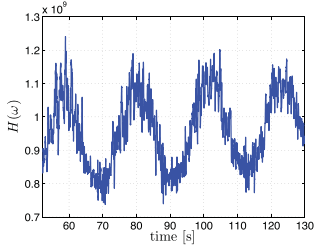


Fig. 23. Second experiment. Behavior of  $H(\mathbf{w})$  while rotating on the spot.

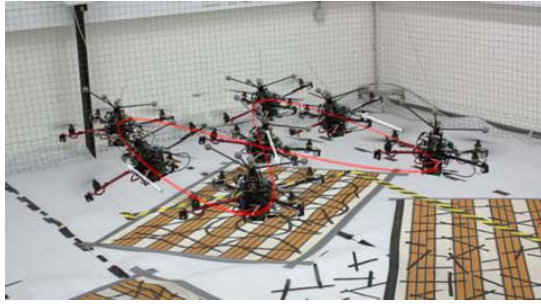


Fig. 24. Third experiment. Overlay of several snapshots of the holocopter while performing eight-shape trajectory.

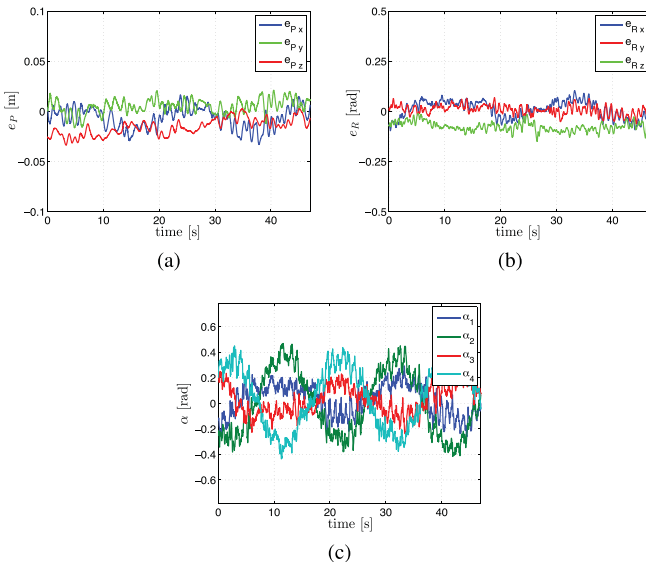


Fig. 25. Third experiment. (a) Position-tracking error  $e_P(t)$ :  $x$  (blue),  $y$  (green), and  $z$  (red). (b) Orientation-tracking error  $e_R(t)$ : roll (blue), pitch (red), and yaw (green). (c) Behavior of the tilting angles  $\alpha_i(t)$ .

flight (blue: roll, green: pitch, red: yaw), and Fig. 18(b) the orientation-tracking error  $e_R(t)$ . The position-tracking error  $e_P(t)$  is shown in Fig. 18(c), with a maximum of  $\max(\|e_P(t)\|) = 0.062$  m. Finally, Fig. 18(d) shows the behavior of the tilting angles  $\alpha_i(t)$  during the maneuver, and Fig. 23 shows the behavior of  $H(\mathbf{w})$ . As clear from the plots, this experiment involving a rotation on the spot still confirms the capabilities of the holocopter and the robustness of the proposed control strategy in coping with all the nonidealities of real-world conditions.



Fig. 26. CAD image of the new prototype with improved mechanics, actuation system, electronics, and an overall reduced mass and inertia.

### C. Eight-Shape Trajectory

This last experiment shows the performance of the holocopter in tracking the same eight-shape trajectory with superimposed sinusoidal rotation described in Sections V-A.2 and V-B.2. Fig. 24 shows an overlay of several snapshots taken during flight.

Fig. 25(a) shows the position-tracking error  $e_P(t)$  of the holocopter while following the trajectory, while Fig. 25(b) shows the orientation-tracking error  $e_R(t)$ . The maximum position error  $\max(\|e_P(t)\|)$  while following the path was approximately 3.9 cm, with  $\text{avg}(\|e_P(t)\|) \approx 2.2$  cm. The maximum orientation errors were 0.10 rad for roll, 0.06 rad for pitch, and 0.15 rad for yaw. Fig. 25(b) shows the behavior of the tilting angles  $\alpha_i(t)$ . Note how these experimental results match very well those of the realistic simulation described in Section V-B.2, thus also confirming the validity of the employed holocopter model. The interested reader is also appreciated to watch the execution of this task in the video attached to this paper.

## VII. CONCLUSION

In this paper, we have presented a novel overactuated quadrotor UAV called holocopter able to achieve full controllability over its 6-dof body pose in space. This design overcomes the typical limitations of standard (underactuated) quadrotor UAVs where only 4 DoF can be independently controlled, namely the body position and yaw angle. The holocopter design, in contrast, allows to actively and individually control the tilting angles of its four propellers, thus granting a total of 4 + 4 available control inputs which (as proven in this paper) yields full controllability over its pose. Several ideal/realistic simulations and experimental results have been reported and discussed to assess the effectiveness of the control strategy developed for the holocopter; despite the various nonidealities of the real prototype with respect to the modeling assumptions, a satisfactory performance has nevertheless been achieved when executing complex maneuvers which would be impossible for standard quadrotor UAVs.

Our future goal is to exploit the holocopter as a flying service robot capable of advanced interaction tasks with the environment. To this end, we are currently developing the second-generation prototype shown in Fig. 26 with the aim of overcoming the limitations of the first prototype discussed in this paper. In particular, we are focusing on improving the holocopter actuation system (see Section IV-C), as well as obtaining a reduced overall weight, better onboard

sensors, higher onboard computational power, and a more robust mechanical design. This will enable better tracking performance and allow for a full exploitation of the holocopter 6-dof motion capabilities in the planned interaction tasks with the environment.

#### ACKNOWLEDGMENT

Part of Heinrich Bülfhoff's research was supported by the Brain Korea 21 PLUS Program through the National Research Foundation of Korea funded by the Ministry of Education. Correspondence should be directed to Heinrich H. Bülfhoff.

#### REFERENCES

- [1] S. Bouabdallah, M. Becker, and R. Siegwart, "Autonomous miniature flying robots: Coming soon!—Research, development, and results," *IEEE Robot. Autom. Mag.*, vol. 13, no. 3, pp. 88–98, Sep. 2007.
- [2] P. Pounds, R. Mahony, and P. Corke, "Modelling and control of a large quadrotor robot," *Control Eng. Pract.*, vol. 18, no. 7, pp. 691–699, 2010.
- [3] R. Mahony, V. Kumar, and P. Corke, "Multirotor aerial vehicles: Modeling, estimation, and control of quadrotor," *IEEE Robot. Autom. Mag.*, vol. 19, no. 3, pp. 20–32, Sep. 2012.
- [4] M.-D. Hua, T. Hamel, P. Morin, and C. Samson, "A control approach for thrust-propelled underactuated vehicles and its application to VTOL drones," *IEEE Trans. Autom. Control*, vol. 54, no. 8, pp. 1837–1853, Aug. 2009.
- [5] M.-D. Hua, T. Hamel, P. Morin, and C. Samson, "Introduction to feedback control of underactuated VTOL vehicles: A review of basic control design ideas and principles," *IEEE Control Syst. Mag.*, vol. 33, no. 1, pp. 61–75, Feb. 2013.
- [6] D. Mellinger, N. Michael, and V. Kumar, "Trajectory generation and control for precise aggressive maneuvers with quadrotors," in *Proc. Int. Symp. Experim. Robot.*, 2010.
- [7] A. Franchi, C. Secchi, M. Ryll, H. H. Bülfhoff, and P. R. Giordano, "Shared control: Balancing autonomy and human assistance with a group of quadrotor UAVs," *IEEE Robot. Autom. Mag.*, vol. 19, no. 3, pp. 57–68, Sep. 2012.
- [8] A. Kushleyev, D. Mellinger, and V. Kumar, "Towards a swarm of agile micro quadrotors," in *Proc. Robot., Sci. Syst.*, Jul. 2012.
- [9] S. Shen, Y. Mulgaonkar, N. Michael, and V. Kumar, "Vision-based state estimation and trajectory control towards high-speed flight with a quadrotor," in *Proc. Robot., Sci. Syst.*, Jun. 2013.
- [10] EU Collaborative Project ICT-248669 AIRobots [Online]. Available: <http://www.airobots.eu>
- [11] EU Collaborative Project ICT-287617 ARCAS [Online]. Available: <http://www.arcas-project.eu>
- [12] L. Gentili, R. Naldi, and L. Marconi, "Modeling and control of VTOL UAVs interacting with the environment," in *Proc. 47th IEEE Conf. Decision Control (CDC)*, Dec. 2008, pp. 1231–1236.
- [13] R. Naldi and L. Marconi, "Modeling and control of the interaction between flying robots and the environment," in *Proc. 8th Int. Fed. Autom. Control (IFAC) Symp. Nonlinear Control Syst. (NOLCOS)*, 2010, pp. 975–980.
- [14] L. Marconi and R. Naldi, "Control of aerial robots: Hybrid force and position feedback for a ducted fan," *IEEE Control Syst. Mag.*, vol. 32, no. 4, pp. 43–65, Aug. 2012.
- [15] P. E. I. Pound, D. R. Bersak, and A. M. Dollar, "Grasping from the air: Hovering capture and load stability," in *Proc. IEEE Int. Conf. Robot. Autom. (ICRA)*, May 2011, pp. 2491–2498.
- [16] Q. Lindsey, D. Mellinger, and V. Kumar, "Construction of cubic structures with quadrotor teams," in *Proc. Robot., Sci. Syst.*, Jun. 2011.
- [17] R. Spica, A. Franchi, G. Oriolo, H. H. Bülfhoff, and P. R. Giordano, "Aerial grasping of a moving target with a quadrotor UAV," in *Proc. IEEE Int. Conf. Intell. Robot. Syst. (IROS)*, Jul. 2012, pp. 4985–4992.
- [18] K. Sreenath and V. Kumar, "Dynamics, control and planning for cooperative manipulation of payloads suspended by cables from multiple quadrotor robots," in *Proc. Robot., Sci. Syst.*, Jun. 2013.
- [19] M. Manubens, D. Devaurs, L. Ros, and J. Cortés, "Motion planning for 6-D manipulation with aerial towed-cable systems," in *Proc. Robot., Sci. Syst.*, Berlin, Germany, Jun. 2013.
- [20] M.-D. Hua, T. Hamel, and C. Samson, "Control of VTOL vehicles with thrust-direction tilting," in *Proc. 19th Int. Fed. Autom. Control (IFAC) World Congr.*, 2014.
- [21] Y. Long and D. J. Cappelleri, "Linear control design, allocation, and implementation for the omnicopter MAV," in *Proc. IEEE Int. Conf. Robot. Autom. (ICRA)*, May 2013, pp. 289–294.
- [22] K. T. Oner, E. Cetinsoy, M. Unel, M. F. Aksit, I. Kandemir, and K. Gulez, "Dynamic model and control of a new quadrotor unmanned aerial vehicle with tilt-wing mechanism," in *Proc. World Acad. Sci., Eng. Technol.*, 2008, pp. 58–63.
- [23] K. T. Oner, E. Cetinsoy, E. Sirimoglu, C. Hancer, T. Ayken, and M. Unel, "LQR and SMC stabilization of a new unmanned aerial vehicle," in *Proc. World Acad. Sci., Eng. Technol.*, Oct. 2009, pp. 554–559.
- [24] R. Voyles and G. Jiang, "Hexrotor UAV platform enabling dexterous interaction with structures—Preliminary work," in *Proc. IEEE Int. Symp. Safety, Security, Rescue Robot. (SSRR)*, Nov. 2012, pp. 1–7.
- [25] F. Kendoul, I. Fantoni, and R. Lozano, "Modeling and control of a small autonomous aircraft having two tilting rotors," *IEEE Trans. Robot.*, vol. 22, no. 6, pp. 1297–1302, Dec. 2006.
- [26] A. Sanchez, J. Escareño, O. Garcia, and R. Lozano, "Autonomous hovering of a noncyclic tiltrotor UAV: Modeling, control and implementation," in *Proc. 17th Int. Fed. Autom. Control (IFAC) Wold Congr.*, Jul. 2008, pp. 803–808.
- [27] F. Forte, R. Naldi, A. Serrani, and L. Marconi, "Control of modular aerial robots: Combining under- and fully-actuated behaviors," in *Proc. IEEE 51st Annu. Conf. Decision Control (CDC)*, Dec. 2012, pp. 1160–1165.
- [28] M. Ryll, H. H. Bülfhoff, and P. R. Giordano, "Modeling and control of a quadrotor UAV with tilting propellers," in *Proc. IEEE Int. Conf. Robot. Autom. (ICRA)*, May 2012, pp. 4606–4613.
- [29] R. Falconi and C. Melchiorri, "Dynamic model and control of an overactuated quadrotor UAV," in *Proc. 10th Int. Fed. Autom. Control (IFAC) Symp. Robot. Control*, 2012, pp. 192–197.
- [30] M. Ryll, H. H. Bülfhoff, and P. R. Giordano, "First flight tests for a quadrotor UAV with tilting propellers," in *Proc. IEEE Int. Conf. Robot. Autom. (ICRA)*, May 2013, pp. 295–302.
- [31] K. P. Valavanis, Ed., *Advances in Unmanned Aerial Vehicles: State of the Art and the Road to Autonomy*. New York, NY, USA: Springer-Verlag, 2007.
- [32] W. Stepniewski and C. Keys, Eds., *Rotary-Wing Aerodynamics*. New York, NY, USA: Dover, 1984.
- [33] G. Fay, *Derivation of the Aerodynamic Forces for the Mesicopter Simulation*. Stanford, CA, USA: Stanford Univ. Press, 2001.
- [34] A. Isidori, *Nonlinear Control Systems*, 3rd ed. New York, NY, USA: Springer-Verlag, 1995.
- [35] A. De Luca, G. Oriolo, and P. R. Giordano, "Kinematic control of nonholonomic mobile manipulators in the presence of steering wheels," in *Proc. IEEE Int. Conf. Robot. Autom. (ICRA)*, May 2010, pp. 1792–1798.
- [36] D. Mellinger and V. Kumar, "Minimum snap trajectory generation and control for quadrotors," in *Proc. IEEE Int. Conf. Robot. Autom. (ICRA)*, May 2011, pp. 2520–2525.
- [37] T. Lee, M. Leok, and N. H. McClamroch, "Geometric tracking control of a quadrotor UAV on SE(3)," in *Proc. 49th IEEE Conf. Decision Control (CDC)*, Dec. 2010, pp. 5420–5425.
- [38] A. De Luca, G. Oriolo, and B. Siciliano, "Robot redundancy resolution at the acceleration level," *Robotica*, vol. 4, no. 2, pp. 97–106, 1992.
- [39] W. A. Wolovich, *Automatic Control Systems*. London, U.K.: Oxford Univ. Press, 1994.



**Markus Ryll** received the B.Sc. degree in mechatronics from Cooperative State University, Karlsruhe, Germany, in 2008, and the M.Eng. degree in medical engineering from the University of Applied Sciences, Ulm, Germany, in 2010, with the master's thesis carried out at the Karolinska Institute, Stockholm, Sweden. He is currently pursuing the Ph.D. degree with the Max Planck Institute for Biological Cybernetics, Tübingen, Germany.

His current research interests include unmanned aerial vehicles, robotics, and human–robot interaction tasks.



**Heinrich H. Bülowhoff** (M'96) received the Ph.D. degree in biology from Eberhard Karls University, Tübingen, Germany, in 1980.

He was a Research Scientist with the Max Planck Institute for Biological Cybernetics, Tübingen, and the Massachusetts Institute of Technology (MIT), Cambridge, MA, USA, from 1980 to 1988. He was an Assistant, Associate, and Full Professor of Cognitive Science with Brown University, Providence, RI, USA, from 1988 to 1993, before becoming the Director of the Department for Human Perception, Cognition and Action at the Max Planck Institute for Biological Cybernetics and a Scientific Member of the Max Planck Society in 1993. He has been an Honorary Professor with Eberhard Karls University since 1996, and is an Adjunct Professor with the Korea University, Seoul, Korea. His current research interests include object recognition and categorization, perception and action in virtual environments, and human–robot interaction and perception.



**Paolo Robuffo Giordano** (M'08) received the M.Sc. degree in computer science engineering in 2001, and the Ph.D. degree in systems engineering in 2008, from the University of Rome "La Sapienza", Rome, Italy.

He spent one year as a Post-Doctoral with the Institute of Robotics and Mechatronics, German Aerospace Center (DLR), Oberpfaffenhofen, Germany, from 2007 to 2008, and from 2008 to 2012 he was a Senior Research Scientist with the Max Planck Institute for Biological Cybernetics, Tübingen, Germany. Since 2012 he has been a CNRS Researcher with the Lagadic Group, Irisa and Inria Bretagne Atlantique, Rennes, France. His research interests span nonlinear control, robotics, planning, haptics and VR applications.